Monthly Notices
of the
ROYAL ASTRONOMICAL SOCIETY

MNRAS **506,** 903–918 (2021)
Advance Access publication 2021 June 11

https://doi.org/10.1093/mnras/stab1669

Prospects of high redshift constraints on dark energy models with the $E_{\rm p,\,i} - E_{\rm iso}$ correlation in long gamma ray bursts

M. Demianski,[1,2]★ E. Piedipalumbo,[3,4]★ D. Sawant[5,6]★ and L. Amati[7]★

[1]*Institute for Theoretical Physics, University of Warsaw, Pasteura 5, PL-02-093 Warsaw, Poland*
[2]*Department of Astronomy, Williams College, Williamstown, MA 01267, USA*
[3]*Dipartimento di Fisica, Università degli Studi di Napoli Federico II, Compl. Univ. Monte S. Angelo, I-80126 Naples, Italy*
[4]*I.N.F.N., Sez. di Napoli, Compl. Univ. Monte S. Angelo, Edificio 6, via Cinthia, I-80126 Napoli, Italy*
[5]*Dipartimento di Fisica e Scienze della Terra, Via Saragat 1, 44122, Ferrara*
[6]*Department of Physics, Indian Institute of Technology Bombay, Powai, Mumbai 400 076, India*
[7]*INAF-IASF, Sezione di Bologna, via Gobetti 101, I-40129 Bologna, Italy*

Accepted 2021 May 28. Received 2021 May 5; in original form 2020 October 6

ABSTRACT

So far large and different data sets revealed the accelerated expansion rate of the Universe, which is usually explained in terms of dark energy. The nature of dark energy is not yet known, and several models have been introduced: a non-zero cosmological constant, a potential energy of some scalar field, effects related to the non-homogeneous distribution of matter, or effects due to alternative theories of gravity. Recently, a tension with the flat ΛCDM model has been discovered using a high-redshift Hubble diagram of supernovae, quasars, and gamma-ray bursts (GRB). Here we use the Union2 type Ia supernovae and GRB Hubble diagram, and a set of direct measurements of the Hubble parameter to explore different dark energy models. We use the Chevallier–Polarski–Linder parametrization of the dark energy equation of state, a minimally coupled quintessence scalar field, and, finally, we consider models with dark energy at early times. We perform a statistical analysis based on the Markov chain Monte Carlo method, and explore the probability distributions of the cosmological parameters for each of the competing models. We apply the Akaike Information Criterion to compare these models: our analysis indicates that an evolving dark energy, described by a scalar field with exponential potential seems to be favoured by observational data.

Key words: gamma-ray burst: general – cosmological parameters – cosmology: observations – dark energy.

1 INTRODUCTION

Starting at the end of the 1990s, observations of high-redshift supernovae of type Ia (SNIa) revealed the accelerated expansion of the Universe (Perlmutter et al. 1998, 1999; Riess et al. 1998, 2007; Astier et al. 2006; Amanullah et al. 2010). This unexpected result has been confirmed by statistical analysis of observations of small-scale temperature anisotropies of the Cosmic Microwave Background Radiation (CMBR) (WMAP 2013; Planck Collaboration XIII 2016). The observed accelerated expansion is usually related to a non-zero cosmological constant or to existence of the so-called dark energy, a cosmic medium with positive energy density but sufficiently large negative pressure, which now provides about 70 per cent of the matter energy in the Universe. The nature of dark energy is, however, not known. The models of dark energy proposed so far range from a non-zero cosmological constant (Peebles 1984; Carroll 2001), to a potential energy of some not yet discovered scalar field (Alam et al. 2003; Sahni et al. 2003), to effects connected with inhomogeneous distribution of matter and averaging procedures (Clarckson & Maartens 2010), or modifications of the Einstein General Theory of Relativity (De Felice & Tsujikawa 2010; Capozzilello & De Laurentis 2011; Clifton et al. 2012; Capozzilello, D'Agostino & Luongo 2019). In the last cases, in general, the effective equation of state (EOS) of dark energy is not constant, but depends on redshift z. Therefore populating the Hubble diagram up to high redshifts remains a primary task to test the consistency of the ΛCDM model (see for instance Lusso et al. 2019; Risaliti & Lusso 2019; Lusso 2020; Lusso et al. 2020, for discussions about the ΛCDM tension) and, therefore, to shine new light on the nature of dark energy. So far dark energy models are poorly tested in the redshift interval between the farthest observed SNIa and that of the Cosmic Microwave Background. In our high redshift investigation we consider the Union2 SNIa data set, and the long gamma-ray burst (GRB) Hubble diagram, constructed by calibrating the correlation between the peak photon energy, $E_{\rm p,\,i}$, and the isotropic equivalent radiated energy, $E_{\rm iso}$ (Demianski et al. 2017a, b). Here we consider an extended $E_{\rm p,\,i} - E_{\rm iso}$ correlation, to take into account possible redshift evolution effects, modelled through power-law terms. It turns out that at least a part of this evolution can be caused by gravitational lensing effects (see for instance, Shirokov et al. 2020). We consider also a sample of 28 direct measurements of the Hubble parameter, compiled by Farooq & Ratra (2013). These measurements are performed through the differential age technique, first suggested by Jimenez & Loeb (2002), which uses red passively evolving galaxies as cosmic

★ E-mail: mde@fuw.edu.pl (MD); ester@na.infn.it (EP); sawant@fe.infn.it (DS); lorenzo.amati@inaf.it (LA)

chronometers. Here we probe the dynamical evolution of dark energy, by considering some proposed so far competing models of dark energy:

(i) an empirically parametrized EOS of dark energy, usually using two or more free parameters. Among all the proposed parametrization forms of the dark energy EOS, we consider the Chevallier–Polarski–Linder (CPL; Chevallier & Polarski 2001; Linder 2003), which is now widely used,

(ii) a quintessence dark energy: a model where a self-interacting scalar field plays the role of dark energy and drives the acceleration (Peebles & Ratra 1988a; Ratra & Peebles 1988b; Tsujikawa 2013),

(iii) early dark energy: models where a non-negligible fraction of dark energy exists already at early stages of evolution of the Universe (Khoraminazad et al. 2020) .

Our statistical analysis is based on the Monte Carlo Markov Chain (MCMC) simulations to simultaneously compute the full probability density functions (PDFs) of all the parameters of interest. The structure of the paper is as follows. In Section 2, we describe the different models of dark energy considered in our analysis. In Section 3, we describe the observational data sets that are used in our analysis. In Section 4, we describe some details of our statistical analysis and present results. In Section 5, we present constrains on dark energy models that could be derived from future GRB Hubble diagram samples. General discussion of our results and conclusions are presented in Section 6.

2 DIFFERENT MODELS OF DARK ENERGY

Although seemingly consistent with the current standard model where the cosmic acceleration is due to the Einstein's cosmological constant, Λ, the precision of current data is not sufficient to rule out an evolving dark energy term. If then the cosmological constant is not responsible for the observed accelerated expansion of the Universe, we are considering some of the proposed models of a dynamical field that is generating an effective negative pressure. Moreover this could also indicate that the cosmological Copernican principle cannot be applied at certain scales, and that radial inhomogeneities could mimic the accelerated expansion. Within the Friedman–Lemaitre–Robertson–Walker (FLRW) paradigm, all possibilities can be characterized, as far as the background dynamics is concerned, by the dark energy EOS, $w(z)$. The main task of observational cosmology is to search for evidence for $w(z) \neq -1$. This is usually done in terms of an appropriate parametrization of the EOS.

2.1 Parametrization of the dark energy EOS

Within the Friedman equations dark energy appears through its effective energy density, $\rho_{\rm de}$, and pressure, $p_{\rm de}$:

$$H^2 = \frac{8\pi G}{3}(\rho_{\rm m} + \rho_{\rm de}), \tag{1}$$

$$\frac{\ddot{a}}{a} = -\frac{4\pi G}{3}\left(\rho_{\rm m} + \rho_{\rm de} + 3p_{\rm de}\right), \tag{2}$$

where a is the scale factor, $H = \dot{a}/a$ the Hubble parameter, and ρ_m is the dark matter energy density. Here and throughout this paper the dot denotes the derivative with respect to the cosmic time, and we have assumed a spatially flat Universe in agreement with what is inferred from the CMBR anisotropy spectrum (Planck Collaboration XIII 2016). The continuity equation for any cosmological fluid is:

$$\frac{\dot{\rho}_i}{\rho_i} = -3H\left(1 + \frac{p_i}{\rho_i}\right) = -3H\left[1 + w_i(t)\right], \tag{3}$$

where the energy density ρ_i, the pressure p_i, and the EOS of each component is defined by $w_i = \frac{p_i}{\rho_i}$. For ordinary non-relativistic matter $w = 0$, and the cosmological constant can be treated as a medium with $w = -1$. Let us recall that $\rho_{\rm m} = Da^{-3}$, where the parameter $D \equiv \rho_{\rm m0} a_0^3$ is determined by the current values of $\rho_{\rm m}$ and a. If we explicitly allow the possibility that the dark energy evolves, the importance of its equation of state is significant and it determines the Hubble function $H(z)$, and any derivation of it as needed to obtain the observable quantities. Actually it turns out that:

$$H(z,\theta) = H_0\sqrt{(1-\Omega_{\rm m})g(z,\theta) + \Omega_{\rm m}(z+1)^3}, \tag{4}$$

where

$$g(z,\theta) = \frac{\rho_{\rm de}(z,\theta)}{\rho_{\rm de}(0)} = e^{3\int_0^z \frac{w(x,\theta)+1}{x+1}\,{\rm d}x},$$

$w(z,\theta)$ is any dynamical form of the dark energy EOS, and $\theta = (\theta_1, \theta_1.., \theta_n)$ are the EOS parameters.

It is worth noting that in equation (4) we are neglecting the radiation term $\Omega_r(1+z)^4$, but in this way we introduce errors much smaller than the observational uncertainties of all our data sets. Of course in the case of the early dark energy, when we have to investigate a dark energy component just in early times, we must include the radiation term.

Using the Hubble function we define the luminosity distance d_L as

$$d_L(z,\theta) = \frac{c}{H_0}(1+z)\int_0^z \frac{{\rm d}y}{H(y,\theta)} \tag{5}$$

$$= \frac{c}{H_0}(1+z)\int_0^z \frac{{\rm d}y}{\sqrt{(1-\Omega_m)g(y,\theta) + \Omega_m(y+1)^3}}. \tag{6}$$

Using the luminosity distance, we can evaluate the distance modulus, from its standard definition (in Mpc):

$$\mu(z) = 25 + 5\log d_L(z,\theta). \tag{7}$$

In this work, we consider the so-called CPL parametrization of the dark energy EOS (Chevallier & Polarski 2001; Linder 2003) given by

$$w(z) = w_0 + w_1 z(1+z)^{-1}, \tag{8}$$

where w_0 and w_1 are real numbers that represent the EOS present value and its overall time evolution, respectively.

2.2 A scalar field quintessence model

One of the more interesting physical realizations of the dark energy is the so-called quintessence, i.e. a self-interacting scalar field minimally coupled with gravity (Peebles & Ratra 1988a; Ratra & Peebles 1988b; Tsujikawa 2013). Such field induces the repulsive gravitational force dynamically, driving the accelerated expansion of the Universe. Moreover, it also influences the growth of structures, arisen from gravitational instability. Quintessence could cluster gravitationally on very large scales ($\simeq$100 Mpc), and leaves an imprint on anisotropy of the microwave background radiation (Caldwell & Steinhardt 1998), and, at smaller scales, its fluctuations are damped and do not modify the evolution equation for the perturbations in the dark matter (Ma et al. 1999). Since redshift space distortions in the clustering of galaxies provide constrains on the growth rate of matter perturbations, $\delta_{\rm m}$, which depend on the scalar field dynamics, and on the scalar field equation of state, it is possible to test quintessence models from this kind of data (see for instance Alcaniz & Lima 2001; Copeland, Sami & Tsujikawa 2006; Bueno Sanchez & Perivolaropoulos 2010, and references therein). Indeed in Demianski

et al. (2005), we showed that some scalar models with exponential potential, including the one used in the present analysis, are fully compatible with the power spectrum of the CMBR anisotropy, and the parameters of large-scale structure determined by the 2-degree Field Galaxy Redshift Survey (2dFGRS). It is worth noting that, in absence of the matter term, it is possible to deeply connect extended theories of gravity, as $f(R)$ theories and scalar tensor theories in the so-called Jordan frame, to minimally coupled scalar field with appropriate self interaction potential. Actually, to any $f(R)$ theory in the so-called Jordan frame, in the Einstein frame corresponds a minimally coupled scalar field, throughout the conformal transformation

$$g_{\mu\nu} \rightarrow \tilde{g}_{\mu\nu} = \Omega^2 g_{\mu\nu},$$

where $\Omega \equiv \exp(\varphi) = \sqrt{f'(R)}$, with a potential given by (Maeda 1989):

$$V(\tilde{\varphi}) = \frac{f(R) - Rf'(R)}{2\,[f'(R)]^2}. \tag{9}$$

Here tilted quantities refer to the Einstein frame and $'$ denotes partial derivative with respect to R. It is worth highlighting, however, that this connection only holds in the absence of a matter term. Indeed, even if it is possible to derive a conformal transformation in presence of a matter term, the self-interaction potential is not expressed as in equation (9), and matter becomes coupled to the scalar field. Therefore the physical equivalence of these two conformally equivalent theories remains an open question in theoretical cosmology (see for instance Ma et al. 1999; Capozziello et al. 2006; Demianski et al. 2008). Many quintessence models have been proposed, considering different kinds of potentials driving the dynamics of the scalar field. Here we take into account the specific class of exponential–type potential; in particular we consider an exponential potential for which general exact solutions of the Friedman equations are known (Rubano & Scudellaro 2002; Demianski et al. 2005; Demianski, Piedipalumbo & Rubano 2011; Piedipalumbo et al. 2012). Assuming that φ is minimally coupled to gravity, the cosmological equations are written as

$$\left(\frac{\dot{a}}{a}\right)^2 = \frac{8\pi G}{3}\left(Da^{-3} + \frac{1}{2}\dot{\varphi}^2 + V(\varphi)\right), \tag{10}$$

$$2\frac{\ddot{a}}{a} + \left(\frac{\dot{a}}{a}\right)^2 = -\frac{8\pi G}{3}\left(\frac{1}{2}\dot{\varphi}^2 - V(\varphi)\right), \tag{11}$$

$$\ddot{\varphi} + 3\left(\frac{\dot{a}}{a}\right)\dot{\varphi} + V'(\varphi) = 0, \tag{12}$$

and $'$ denotes partial derivative with respect to φ. Here we consider the potential analysed in Demianski et al. (2011) and Piedipalumbo et al. (2012),

$$V(\varphi) \propto \exp\left\{-\sqrt{\frac{3}{2}}\varphi\right\}, \tag{13}$$

for which the general exact solution exists: actually it turns out that

$$a^3(t) = \frac{t^2}{2}[(3\mathcal{H}_0 - 2)t^2 + 4 - 3\mathcal{H}_0], \tag{14}$$

$$H(t) = \frac{2\left(2(3\mathcal{H}_0 - 2)t^2 + 4 - 3\mathcal{H}_0\right)}{3t\left((3\mathcal{H}_0 - 2)t^2 + 4 - 3\mathcal{H}_0\right)}, \tag{15}$$

$$\Omega_M = \frac{(4 - 3\mathcal{H}_0)\left((3\mathcal{H}_0 - 2)t^2 + 4 - 3\mathcal{H}_0\right)}{[2(3\mathcal{H}_0 - 2)t^2 + 4 - 3\mathcal{H}_0]^2}, \tag{16}$$

$$\Omega_\varphi = \frac{(3\mathcal{H}_0 - 2)t^2\left(4(3\mathcal{H}_0 - 2)t^2 + 3(4 - 3\mathcal{H}_0)\right)}{[2(3\mathcal{H}_0 - 2)t^2 + 4 - 3\mathcal{H}_0]^2} \tag{17}$$

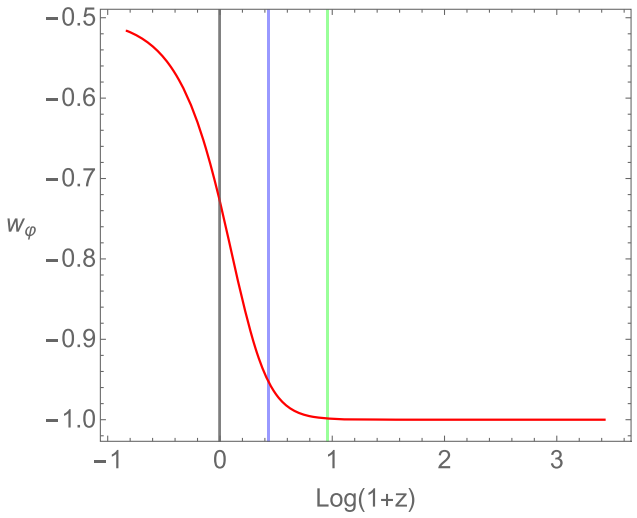

Figure 1. Redshift dependence of the equation of state parameter w_φ corresponding to the best-fitting value of H_0, as illustrated in the statistical analysis section: we see that w_φ smoothly transits between two asymptotic constant values. The vertical lines indicate respectively the SNIa (blue line) and the GRB range of redshift (green line).

$$\varphi(t) = -\sqrt{\frac{2}{3}}\log\left(\frac{6.48}{(3\mathcal{H}_0 - 2)\,t^2 - 3\mathcal{H}_0 + 4}\right), \tag{18}$$

where $\mathcal{H}_0$ is a constant. In order to determine the integration constants we set the present time $t_0 = 1$, so we are using the age of the universe as a unit of time, so $a_0 = a(1) = 1$, which is a standard choice, and finally $\mathcal{H}_0 = H(1)$. Because of our choice of time unit $\mathcal{H}_0$ does not have the same value as the standard Hubble constant H_0. In this model, all the basic cosmological parameters can be written in terms of $\mathcal{H}_0$ only, so we find that:

$$\Omega_{M_0} \equiv \Omega_M(t = 1) = \frac{2(4 - 3\,\mathcal{H}_0)}{9\,\mathcal{H}_0^2}, \tag{19}$$

$$\Omega_{\varphi_0} \equiv \Omega_\varphi(t = 1) = \frac{(3\,\mathcal{H}_0 - 2)\,(3\,\mathcal{H}_0 + 4)}{9\,\mathcal{H}_0^2}. \tag{20}$$

The scalar field EOS evolves with time and the parameter w is given by

$$w_\varphi = -\frac{1}{2} + \frac{3(3\,\mathcal{H}_0 - 4)}{6(4 - 3\,\mathcal{H}_0) + 8\,(3\,\mathcal{H}_0 - 2)\,t^2}, \tag{21}$$

so that today we have

$$w_{\varphi_0} = -\frac{8 - 3\mathcal{H}_0}{4 + 3\mathcal{H}_0}. \tag{22}$$

As we see in Fig. 1, the scalar field EOS in the past is equal to $w_\varphi = -1$ so that the dark energy behaves as a subdominant cosmological constant, but only recently has started dominating the expansion of the universe, as illustrated in Fig. 2. It turns out that it undergoes a transition from a subdominant phase, during the matter-dominated era, to a dominant phase, associated to the present accelerated expansion. It is clear that extending the Hubble diagram beyond the SNIa range of redshift allows us to fully investigate the transition of the EOS from $w_\phi = -1$ to its present value.

2.3 Early dark energy

In this section, we consider some proposed cosmological models that allow a non-negligible amount of dark energy at early times (Doran

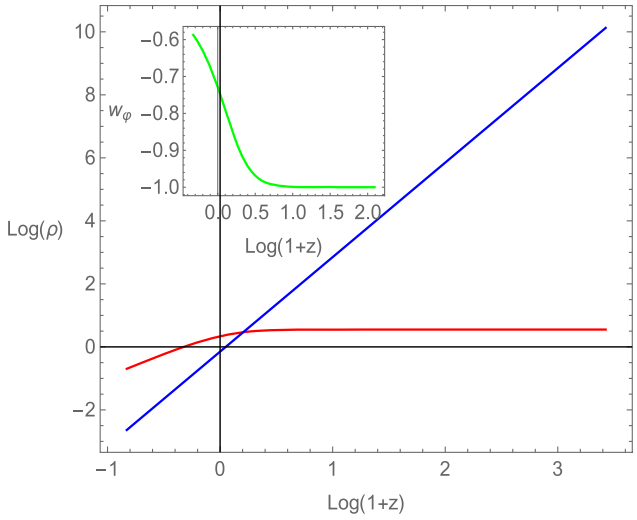

Figure 2. The scalar field density energy ρ_φ (red line) is compared with the matter density (blue line): we see the transition from a subdominant phase, during the matter-dominated era, to a dominant phase, at the present accelerated expansion. It turns out that the range of redshifts of this transition corresponds to the passage of the equation of state from $w_\varphi = -1$ to its present value.

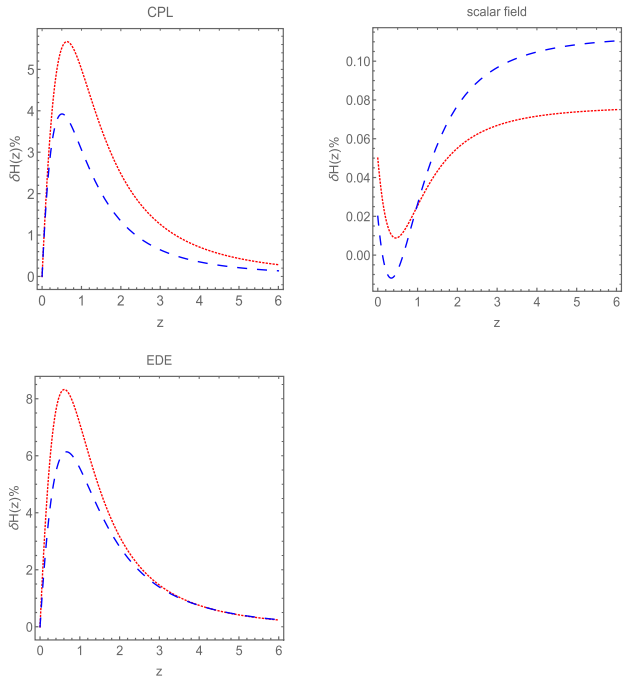

Figure 3. We show relative residual curves of $\frac{H(z,\Lambda)-H(z,\theta)}{H(z,\Lambda)}$ for all considered competing models described above. For the flat ΛCDM model we take $\Omega_m = 0.3$, and $H_0 = 70$. For other models the values of the parameters have been chosen in order to highlight the differences between models. In particular, for the CPL model $\Omega_{\rm m} = 0.3$, $h = 0.7$, $w_0 = -1.2$, $w_1 = 0.2$ (red line), and $\Omega_{\rm m} = 0.3$, $h = 0.7$, $w_0 = -1.2$, $w_1 = -0.2$ (blue line); for the EDE model $\Omega_{\rm m} = 0.3$, $h = 0.7$, $w_0 = -1$, $\Omega_{\rm e} = 0.08$, $\omega_\gamma = 2.47\ 10^{-5}$ (red line), $\Omega_{\rm m} = 0.27$, $h = 0.7$, $w_0 = -1$, $\Omega_{\rm e} = 0.03$, $\omega_\gamma = 2.47\ 10^{-5}$(blue line). For the scalar field model $\mathcal{H}_0 = 0.94$ (red line) and $\mathcal{H}_0 = 0.98$.

& Robbers 2006): they are often connected with the existence of scaling or attractor-like solutions, in which the dark energy density follows the density of the dominant component of matter-energy in the Universe. These models naturally predict a non-vanishing dark energy fraction of the total energy at early times, Ω_e, which should be substantially smaller than its present value. Therefore these models need an *exit mechanism*, allowing the scaling solutions to end in the recent cosmological past, in order to trigger a dark energy dominant era. A large class of models of this type has been proposed (Karwal & Kamionkowski 2016; Niedermann & Sloth 2020). Since the main parameter of an early dark energy model is Ω_e, it parametrizes the evolution of dark energy. In different parametrizations Ω_e have been estimated from several observations, as nucleosynthesis, structure formation, or the peak separation in the power spectrum of the cosmic microwave radiation anisotropy (Doran, Lilley & Wetterich 2002; Doran & Robbers 2006; Das et al. 2011; Di Valentino 2021). Following Doran & Robbers (2006) and Pettorino, Amendola & Wetterich (2013) we use parametrized representation of the dark energy density fraction, $\Omega_{\rm de}$, which depends on the present matter fraction, $\Omega_{\rm m}$, the early dark energy density fraction, $\Omega_{\rm e}$, and the present dark energy equation of state w_0:

$$\Omega_{\rm de}(z,\Omega_{\rm m},\Omega_{\rm e},w_0) = \frac{\Omega_{\rm e}\left((z+1)^{3w_0}-1\right)-\Omega_m+1}{\Omega_m(z+1)^{-3w_0}-\Omega_m+1} + \Omega_{\rm e}\left(1-(z+1)^{3w_0}\right). \quad (23)$$

It turns out that in these models the Hubble function takes the form:

$$H^2(z,\Omega_{\rm m},\Omega_{\rm e},w_0,\Omega_\gamma,N_{\rm eff}) = \Omega_{\rm de}(z,\Omega_{\rm m},\Omega_{\rm e},w_0) + \Omega_{\rm m}(z+1)^3+\Omega_\gamma(z+1)^4 \times\left(\frac{7}{8}\left(\frac{4}{11}\right)^{\frac{4}{3}}N_{\rm eff}+1\right). \quad (24)$$

Here $N_{\rm eff}$ is defined so that the total relativistic energy density (including neutrinos and any other dark radiation) is given in terms of the photon density ρ_γ at $T \ll 1$ MeV by the relation:

$$\rho = N_{\rm eff}\frac{7}{8}\left(\frac{4}{11}\right)^{\frac{4}{3}}\rho_\gamma. \quad (25)$$

In this equation $N_{\rm eff} = 3$ for three standard neutrinos that were thermalized in the early Universe and decoupled well before electron–positron annihilation. Moreover $\Omega_\gamma = \omega_\gamma h^{-2}$, and we set $\omega_\gamma = 2.47\ 10^{-5}$. In Figs 3 and 4, we plot relative residual curves of $\frac{H(z,\Lambda)-H(z,\theta)}{H(z,\Lambda)}$, and $\frac{\mu(z,\Lambda)-\mu(z,\theta)}{\mu(z,\Lambda)}$, for all the competing models described above, where $H(z,\Lambda)$ is the Hubble function in the standard flat ΛCDM model, and $H(z,\theta)$ is the Hubble function in each of the other models parametrized by θ. We plot also curves of $\frac{\mu(z,\Lambda)-\mu(z,\theta)}{\mu(z,\Lambda)}$ for the CPL model and scalar field models: it turns out that the range of redshifts larger than $z = 1$ is very important to break degeneracies among the flat standard ΛCDM and other models considered in this paper. The values of the parameters have been chosen in order to highlight the differences among models.

3 OBSERVATIONAL DATA

In our analysis, we use the SNIa and GRB Hubble diagrams, and a list of 28 direct $H(z)$ measurements, compiled by Farooq & Ratra (2013).

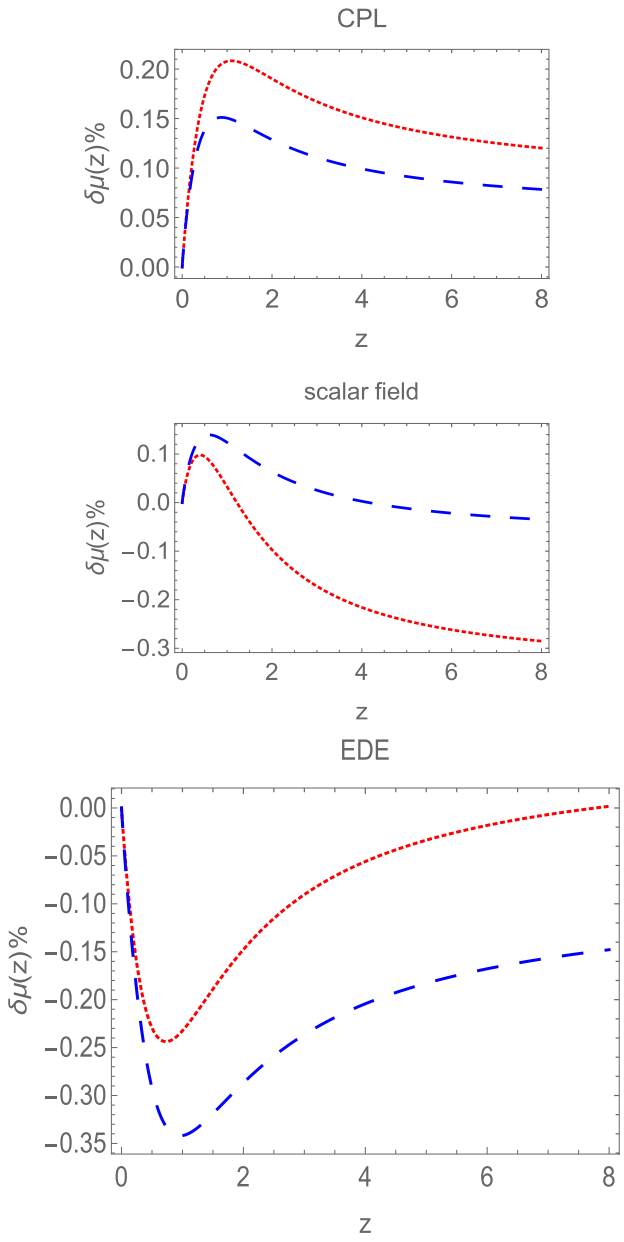

Figure 4. We show relative residual curves of $\frac{\mu(z,\Lambda)-\mu(z,\theta)}{\mu(z,\Lambda)}$ for all our considered models described above. For the flat ΛCDM model we take $\Omega_m = 0.3$, and $H_0 = 70$. For other models the values of parameters have been chosen as in Fig. 3. For the EDE model we take $\Omega_m = 0.3$, $h = 0.7$, $w_0 = -1$, $\Omega_e = 0.08$, $\omega_\gamma = 2.47\ 10^{-5}$ (red line), and $\Omega_m = 0.27$, $h = 0.7$, $w_0 = -1$, $\Omega_e = 0.03$, $\omega_\gamma = 2.47\ 10^{-5}$(blue line).

3.1 Supernovae

SNIa observations gave the first strong indication that now the expansion rate of the Universe is accelerating. First results of the SNIa teams were published in Riess et al. (1998) and Perlmutter et al. (1999). Here we consider the recently updated Supernovae Cosmology Project Union 2.1 compilation (Suzuki et al. (The Supernova Cosmology Project) 2012), which is an update of the original Union compilation. The Union2.1 data set is one of the largest compilations of supernovae of type Ia, originally consisting of 833 SNIe drawn from different samples, and reduced to 580 after several selection criteria. It spans the redshift range $0.015 \leq z \leq 1.4$. To compute the χ^2 function related to the distance modulus, we can easily relate the apparent magnitude $m(z)$ to the so-called Hubble free luminosity distance $D_L(z) = H_0 d_L(z)$ through the relation:

$$m_{\rm th}(z) = \bar{M} + 5\log_{10} D_L(z). \tag{26}$$

Here $\bar{M}$ is the zero-point offset, it depends on the absolute magnitude M and on the present value of the Hubble parameter H_0:

$$\bar{M} = M - 5\log_{10} h + 42.38, \tag{27}$$

where M is the absolute magnitude. The cosmological model parameters can be determined by minimizing the quantity

$$\chi^2_{\rm SNIa}(\{\theta_p\}) = \sum_{i=1}^{N} \frac{(\mu_{\rm obs}(z_i) - \mu_{\rm th}(z_i, \{\theta_p\}))^2}{\sigma^2_{\mu\, i}}. \tag{28}$$

Here $\sigma^2_{\mu\, i} = \tilde{\sigma}^2_{\mu\, i} + \sigma^2_{\rm int}$, where $\sigma_{\rm int}$ is a fit parameter; in our statistical analysis we will marginalize over $\sigma_{\rm int}$. The theoretical distance modulus is defined as

$$\mu_{\rm th}(z_i, \{\theta_p\}) = 5\log_{10} D_L(z_i, \{\theta_p\}) + \nu_0, \tag{29}$$

where $\nu_0 = 42.38 - 5\log_{10}h$, and $\{\theta_p\}$ denotes the set of parameters that appear in different dark energy models (Nesseris & Perivolaropoulos 2005). For example, in the case of a flat CPL model $\{\theta_p\} = \{\Omega_m, w_0, w_1\}$.

3.2 Gamma-ray bursts

GRBs are visible up to high redshifts thanks to the enormous energy that they release, and thus may be good candidates for our high-redshift cosmological investigation (see for instance, Lin et al. 2015; Izzo et al. 2015; Dainotti et al. 2016; Amati, Sawant & Della Valle 2016a; Lin, Li & Chang 2016a, b; Si et al. 2018; Wei & Wu 2018; Fana Dirirsa et al. 2019; Khadka & Ratra 2020; Zhao et al. 2020), or (Khadka & Ratra 2020; Zhao et al. 2020; Cao et al. 2021; Muccino et al. 2021b). However, GRBs may be everything but standard candles since their peak luminosity spans a wide range, even if there have been many efforts to make them distance indicators using some empirical correlations of distance-dependent quantities and rest-frame observables (Amati et al. 2008).

Actually GRBs show non-thermal spectra which can be empirically modelled with the Band function (Band 1993), which is a smoothly broken power law with parameters α, the low-energy spectral index, γ, the high energy spectral index, and the *roll-over* energy E_0. Their spectra show a peak corresponding to a value of the photon energy $E_p = E_0(2+\alpha)$; indeed it turns out that for GRBs with measured spectrum and redshift it is possible to evaluate the intrinsic peak energy, $E_{p,i} = E_p(1+z)$ and the isotropic equivalent radiated energy, defined as:

$$E_{\rm iso} = 4\pi d_L^2(z,\theta)\,(1+z)^{-1} \int_{1/(1+z)}^{10^4/(1+z)} E N(E) {\rm d}E. \tag{30}$$

Here $N(E)$ is the Band function:

$$N(E) = \begin{cases} A\left(\frac{E}{100keV}\right)^{\alpha_B} \exp\left(-\frac{E}{E_0}\right), (\alpha_B)\, E_0 \geq E, \\ A\left(\frac{(\alpha_B-\beta_B)E}{100keV}\right)^{\alpha_B-\beta_B} \exp(\alpha_B-\beta_B)\left(\frac{E}{100keV}\right)^{\beta_B}, \\ (\alpha_B-\beta_B)\, E_0 \leq E. \end{cases}$$

Even if $E_{p,i}$ and $E_{\rm iso}$ span several orders of magnitude, it turned out that they are strongly correlated, according to the relation (Amati

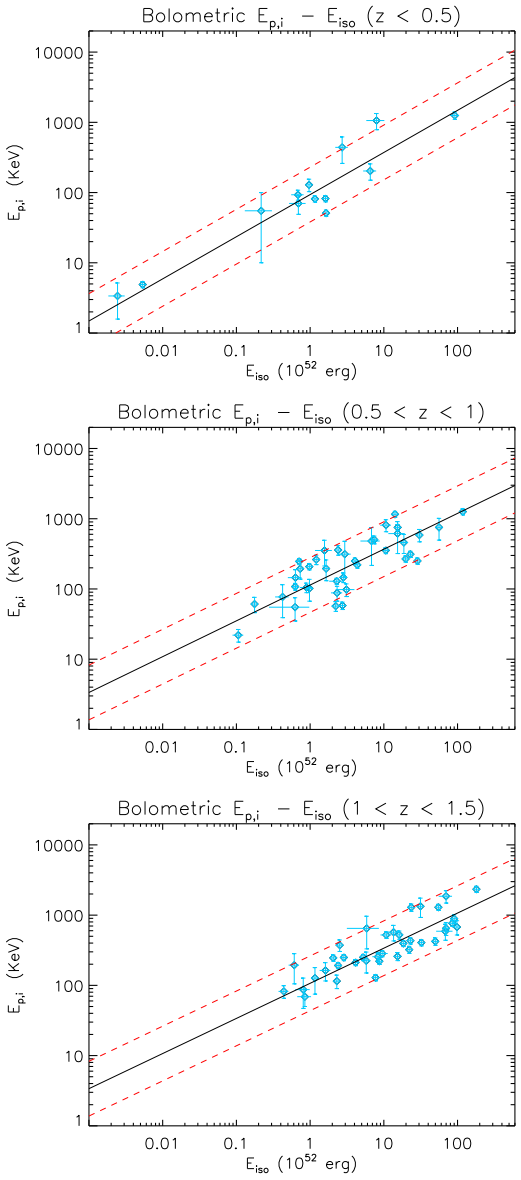

Figure 5. Dependence of time integrated bolometric $E_{p,i}$–$E_{\rm iso}$ correlation on different redshift ranges within the region explored by SNIa Hubble diagram.

et al. 2002).

$$\log\left(\frac{E_{\rm iso}}{1\ {\rm erg}}\right) = b + a\log\left[\frac{E_{\rm p,i}(1+z)}{300\ {\rm keV}}\right], \tag{31}$$

where a and b are constants. This correlation, as other correlations, is characterized by an extra-Poissonian scatter, $\sigma_{\rm int}$, distributed around the best-fitting law. It is clear from equations (30) and (31) that it is possible to use GRBs to investigate cosmological models, if we can calibrate the $E_{\rm p,\,i} - E_{\rm iso}$ correlation in a model-independent way, overcoming the so-called circularity problem, which affects the estimation of the luminosity distance from all the GBR correlations. Actually it turns out that GRBs can be used as cosmological tools through the $E_{\rm p,\,i} - E_{\rm iso}$ correlation; however the computation of $E_{\rm iso}$ is based on a fiducial cosmological model. Different and alternative techniques have been recently developed in literature (see for instance Kodama et al. 2008; Liang et al. 2008; Wei 2010; Izzo et al. 2015; Lin et al. 2015; Wang, Dai & Liang 2015; Amati et al. 2019; ; Luongo & Muccino 2021; Montiel, Cabrera & Hidalgo 2021): here we standardize our GRB data set updating a method previously adopted, as discussed in a later section. The $E_{\rm p,\,i} - E_{\rm iso}$ data sample used in this analysis was build up by Amati and Sawant, they collected the spectral information of GRBs with measured redshift from 1997 February to 2015 October (Amati et al. 2016a). This data base includes redshift z, both energy indices α and γ, the peak energy $E_{\rm p,\,i}$ computed from the break energy E_0, t_{90}, exposure time, the fluence and the value of peak flux. The redshift distribution covers a broad range $0.033 \leq z < 9.0$, thus extending far beyond that of type Ia SN $z \leq 1.7$. For the oldest GRBs (BeppoSAX, BATSE, HETE-2) and other GRBs up to mid-2008, the data were adapted from Amati et al. (2008). As already discussed in (Demianski et al. 2017a), the criteria behind selecting the measurements from a particular mission are based on the following conditions:

(1) We concentrated on observations for which the exposure time was at least 2/3rd of the whole event duration.

(2) Given the broad energy band and good calibration, Konus-WIND and Fermi/GBM were chosen whenever available. For Konus-WIND, the measurements were taken from the official catalogue (Ulanov et al. 2005) and from GCN archives (*<urlhref = "http: //gcn.gsfc.nasa.gov/gcn3 − circulars.html" > http: //gcn.gsfc.nasa.gov/gcn3 − circulars.html < /url >*). In the case of Fermi/GBM, the observations were derived from Gruber (2012) and from several other papers, as, for instance, Ghirlanda et al. (2004). The observations from SUZAKU were not considered as the uncertainties in the calibration are higher and also because it works in a narrow energy band.

(3) The SWIFT BAT observations were chosen when no other preferred missions (Konus-WIND, Fermi/GBM) were able to provide information. They were considered only for GRBs with the value of $E_{\rm p,\,obs}$ that was within the energy band of the instrument. For Swift GRBs, the $E_{\rm p,\,i}$ value derived from BAT spectral analysis alone were conservatively taken from the results reported by the BAT team (Sakamoto et al. 2008). The GCN circulars were also used when needed.

When more than one mission provides good observations based on these criteria, the values and uncertainties of all those observations (hence more than one set for some finely observed GRBs) are taken into account. When the observations were to be included in the data sample, it has been checked that the uncertainty on any value is not below 10 per cent in order to account for the instrumental capabilities, etc. So, when the error was lower, it has been assumed to be 10 per cent. When available, the Band model (Band 1993) was considered since the cut-off power-law tends to overestimate the value of $E_{\rm p,\,i}$. GRBs have been observed by different detectors that are characterized by different thresholds and spectroscopic sensitivity, therefore they can spread relevant selection biases in the observed correlation. This is ongoing debated topic: in the past, there were claims that a large fraction (70 − 90 per cent) of BATSE GRBs without redshift is inconsistent with the correlation for any redshift (Band & Preece 2005; Nakar & Piran 2005). However other authors (Ghirlanda et al. 2008; Nava et al. 2011) showed that, in fact, most BATSE GRBs with unknown redshift were consistent with the $E_{\rm p,\,i} - E_{\rm iso}$ correlation. We also note that inconsistency of a high percentage of GRBs of unknown redshift would imply that most GRBs with known redshift should also be inconsistent with the $E_{\rm p,\,i} - E_{\rm iso}$ relation, and this fact was never observed. Moreover, Amati, Frontera & Guidorzi (2009) showed that the normalization of the correlation varies only marginally for GRBs observed by different instruments with different sensitivities and energy bands, while in other papers as, for instance, Ghirlanda, Nava & Ghisellini (2010) and Amati et al. (2016a) it is shown that the parameters of the correlations are

Table 1. Dependence of the $E_{p,i} - E_{iso}$ correlation on different redshift bins.

Dependence on redshift bins				
$E_{p,i} - E_{iso}$ correlation	Total GRBs	Normalization	Slope	Scatter
$z < 0.5$	13	1.97 ± 0.07	0.60 ± 0.06	0.201 ± 0.052
$0.5 < z < 1$	38	2.05 ± 0.05	0.51 ± 0.07	0.238 ± 0.032
$1 < z < 1.5$	38	2.02 ± 0.06	0.50 ± 0.05	0.172 ± 0.025
$1.5 < z < 2$	28	1.95 ± 0.16	0.56 ± 0.11	0.230 ± 0.041
$2 < z < 2.5$	28	2.13 ± 0.11	0.44 ± 0.07	0.174 ± 0.031
$2.5 < z < 3$	16	1.78 ± 0.11	0.68 ± 0.08	0.101 ± 0.031
$3 < z < 3.5$	13	1.99 ± 0.13	0.55 ± 0.10	0.135 ± 0.048
$3.5 < z < 4$	7	2.16 ± 0.15	0.44 ± 0.10	0.069 ± 0.008
$4 < z$	12	2.06 ± 0.13	0.51 ± 0.11	0.116 ± 0.058

Table 2. Dependence of the $E_{p,i} - E_{iso}$ correlation on different energy bins (based on various satellite missions).

Dependence on energy bins				
$E_{p,i} - E_{iso}$ correlation	Total GRBs	Normalization	Slope	Scatter
BeppoSAX (2–700 keV)	11	2.11 ± 0.08	0.48 ± 0.08	0.138 ± 0.057
HETE–2 (2–500 keV)	18	1.88 ± 0.06	0.51 ± 0.06	0.133 ± 0.041
Konus–WIND (20 keV–10 MeV)	72	2.03 ± 0.06	0.54 ± 0.04	0.168 ± 0.019
SWIFT (15–150 keV)	32	1.96 ± 0.03	0.55 ± 0.04	0.113 ± 0.031
FERMI (10–30 MeV)	51	2.11 ± 0.06	0.45 ± 0.05	0.236 ± 0.026

independent of redshift. If the whole GRB sample is divided into redshift bins, as shown in Table 1, Figs 5and 6; it turned out that the possible evolutionary effects are within the intrinsic scatter and, therefore, do not affect the correlation. Similar results were obtained in Dainotti & Amati (2018); Demianski et al. (2017a), and Amati & Della Valle (2013); Demianski & Piedipalumbo (2011).

Furthermore, the *Swift* satellite, thanks to its capability of providing quick and accurate localization of GRBs, thus reducing the selection effects in the observational chain leading to the estimate of GRB redshift, has further confirmed the reliability of the $E_{p,i} - E_{iso}$ correlation (Amati et al. 2009; Ghirlanda et al. 2010; Amati & Dichiara 2013; Martone et al. 2017; Amati et al. 2019). If one dividethe GRB sample on the basis of different high energy satellite missions, it turns out that the correlation always remains within the same $E_{p,i} - E_{iso}$ fit parameters range (slope ~ 0.5), as it can be seen from Table 2, and Figs 7–9.

Moreover, based on time-resolved analysis of BATSE, BeppoSAX, and Fermi GRBs, it was found that the $E_{p,i} - E_{iso}$ correlation also holds within each single GRB with normalization and slope consistent with those obtained with time-averaged spectra and energetics/luminosity (Lu et al. 2012; Basak & Rao 2013; Frontera et al. 2013), confirming the physical origin of the correlation, and providing clues to its explanation. Therefore, it turns out that, at the present stage, the fit values of the $E_{p,i} - E_{iso}$ correlation parameters are marginally affected by selection and/or evolutionary effects, which are less than the intrinsic dispersion (Amati & Della Valle 2013; Amati et al. 2016a; Demianski et al. 2017a; Dainotti & Amati 2018; Sawant & Amati 2018).

3.2.1 *Calibrating the* $E_{p,i} - E_{iso}$ *correlation and fitting its parameters*

Here we update a local regression technique, inspired by the standardization of the SNIa with Cepheid variables, and based on Union 2.1 SNIa sample, which we adopted in previous works (Demianski et al. 2017a, b; Demianski & Piedipalumbo 2011). We actually consider a sort of *extended* $E_{p,i} - E_{iso}$ correlation, introducing in the calibration terms representing the z-evolution, which are assumed to be power-law functions: $g_{iso}(z) = (1+z)^{k_{iso}}$ and $g_p(z) = (1+z)^{k_p}$, so that $E'_{iso} = \frac{E_{iso}}{g_{iso}(z)}$ and $E'_{p,i} = \frac{E_{p,i}}{g_p(z)}$ are the de-evolved quantities (see also Shirokov et al. 2020). Therefore we consider a correlation with three parameters a, b, and $k_{iso} - ak_p$:

$$\log\left[\frac{E_{iso}}{1\ \mathrm{erg}}\right] = b + a\log\left[\frac{E_{p,i}}{300\ \mathrm{keV}}\right] + \left(k_{iso} - ak_p\right)\log(1+z). \quad (32)$$

We can simplify the redshift dependence term in equation (32), introducing a single average coefficient γ:

$$\log\left[\frac{E_{iso}}{1\ \mathrm{erg}}\right] = b + a\log\left[\frac{E_{p,i}}{300\ \mathrm{keV}}\right] + \gamma\log(1+z). \quad (33)$$

Calibrating this 3D relation means determining the coefficients a, b, and γ and the intrinsic scatter σ_{int}. It is worth noting that low values of γ would indicate negligible evolutionary effects. In order to calibrate our de-evolved relation, we consider a 3D Reichart likelihood:

$$L^{3D}_{Reichart}(a,\gamma,b,\sigma_{int}) = \frac{1}{2}\frac{\sum\log\left(\sigma^2_{int}+\sigma^2_{y_i}+a^2\sigma^2_{x_i}\right)}{\log(1+a^2)} + \frac{1}{2}\sum\frac{(y_i - ax_i - \gamma z_i - b)^2}{\sigma^2_{int}+\sigma^2_{x_i}+a^2\sigma^2_{x_i}}. \quad (34)$$

We maximized our likelihood with respect to a and γ since b can be evaluated analytically by solving the equation

$$\frac{\partial}{\partial b}L^{3D}_{Reichart}(a,k_{iso},\alpha,b,\sigma_{int}) = 0, \quad (35)$$

we obtain

$$b = \left[\sum\frac{y_i - ax_i - \gamma z_i}{\sigma^2_{int}+\sigma^2_{y_i}+a^2\sigma^2_{x_i}}\right]\left[\sum\frac{1}{\sigma^2_{int}+\sigma^2_{y_i}+a^2\sigma^2_{x_i}}\right]^{-1}. \quad (36)$$

We also used the MCMC method to maximize the likelihood and ran five parallel chains and the Gelman–Rubin convergence test. We obtain $a = 1.92 \pm 0.09$, $b = 52.7^{+0.04}_{-0.03}$, $\sigma_{int} = 0.35^{+0.04}_{-0.05}$, $\gamma = -0.07 \pm 0.14$, thus confirming that the evolutionary effects, not included in the intrinsic dispersion, can be, at this stage, neglected, as shown in Fig. 10.

3.2.2 *Further investigations on the calibration of the* $E_{p,i} - E_{iso}$ *correlation*

In this section, we discuss some aspects related to the calibration of the $E_{p,i} - E_{iso}$ relation, and its impact on reliability of the GRBs as distance indicators. Actually, we apply some filters on $E_{p,i}$ and E_{iso}, reducing the sample to 60 objects, as shown in Figs 11 and 12, where the $E_{p,i}$ and E_{iso} are *homogeneously* distributed in the sample. Note that the measured values of $E_{p,i}$ and E_{iso} are not systematically larger at lower redshift than at higher redshifts.

From the Reichart likelihood analysis we find that $a = 2.0^{+0.14}_{-0.13}$, $b = 52.5^{+0.04}_{-0.03}$, $\sigma_{int} = 0.38 \pm 0.06$, $\gamma = 0.02 \pm 0.09$. The fit values of the correlation parameters are fully compatible (at 3σ) with the results obtained from the full data set. Moreover it is worthwhile to note that we have been forced to limit our analysis to the redshfit range $0.015 \leq z \leq 1.414$, where we apply our calibration technique. In order to extend our analysis to a wide range of redshifts we build up a further calibration procedure which updates the procedure described in Demianski & Piedipalumbo (2011) and Demianski et al. (2017b),

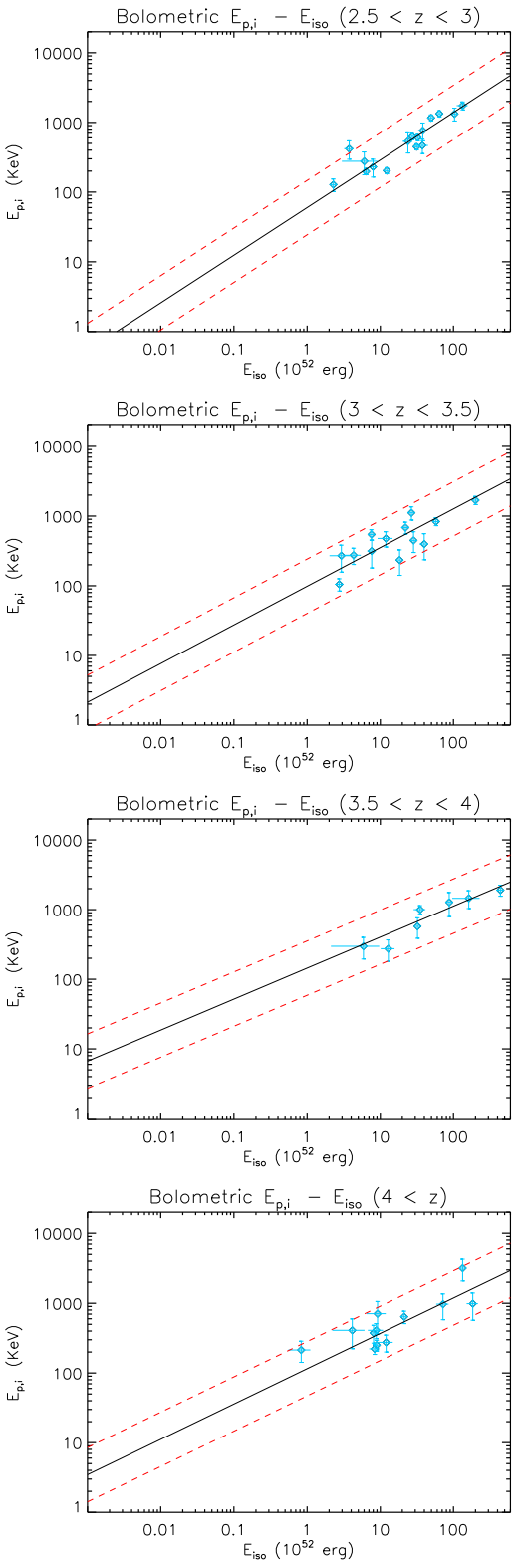

Figure 6. Dependence of time integrated bolometric $E_{p,i}$–$E_{\rm iso}$ correlation on different redshift ranges beyond the SNIa Hubble diagram.

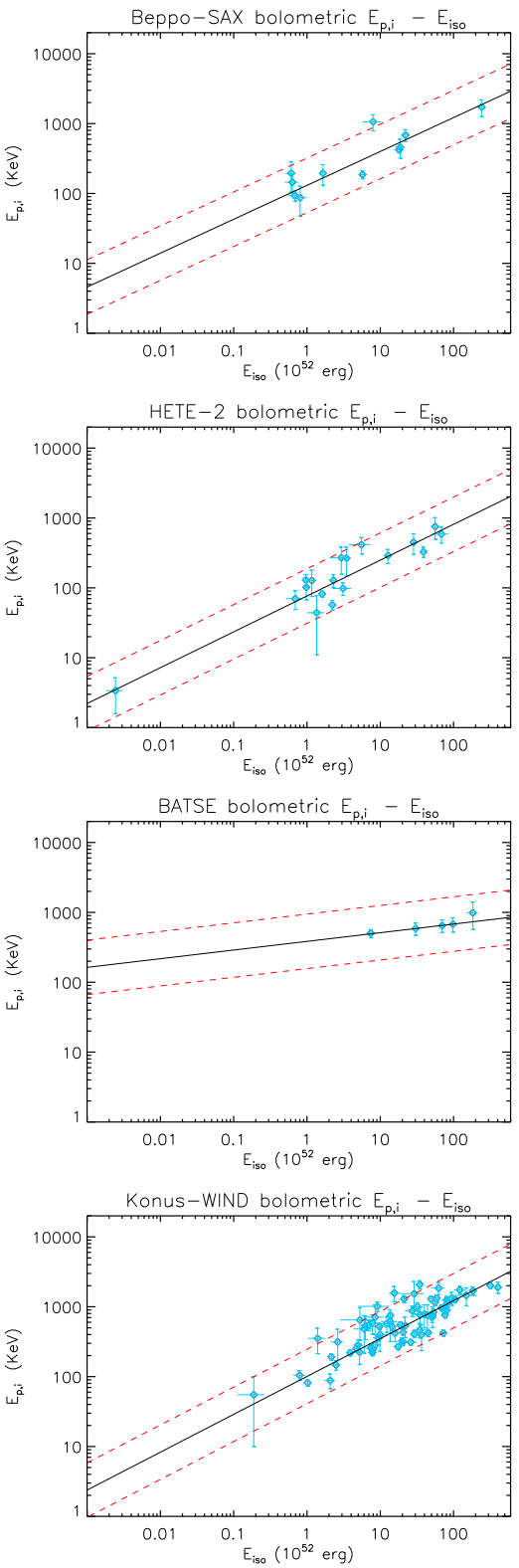

Figure 7. Dependence of the $E_{p,\,i}$ – $E_{\rm iso}$ correlation on different energy ranges (based on various satellite missions).

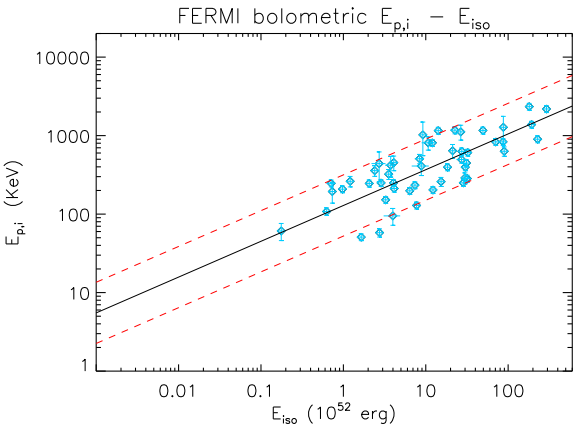

Figure 8. $E_{p,\,i} - E_{\rm iso}$ correlation from Fermi mission.

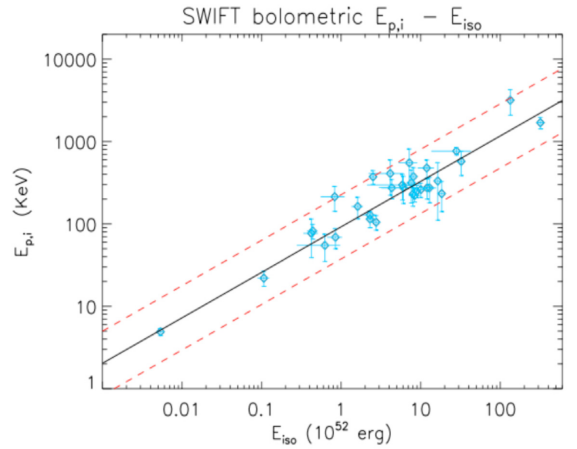

Figure 9. $E_{p,\,i} - E_{\rm iso}$ correlation from *Swift*.

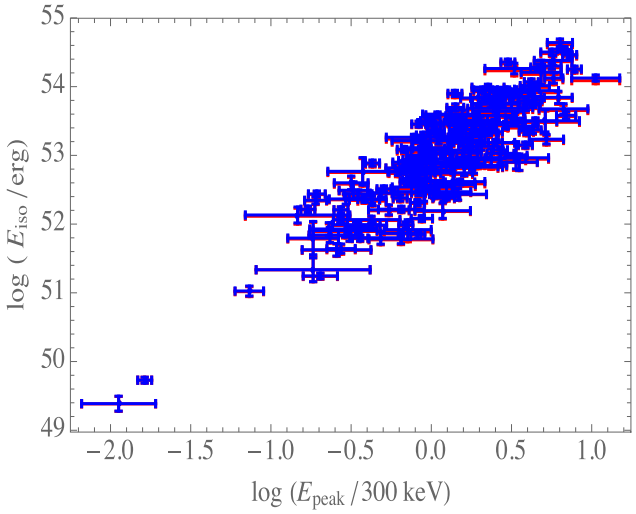

Figure 10. De-evolved (red points) and evolved/original $E_{p,\,i} - E_{\rm iso}$ correlation (blue points); there is no noticeable evolution.

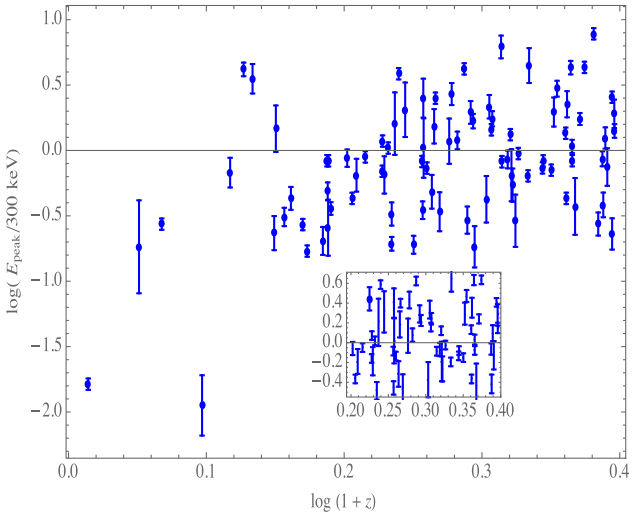

Figure 11. Redshift distribution of $\log E_{\rm p,\,i}/(300\,{\rm keV})$ for the subsample used for our calibration.

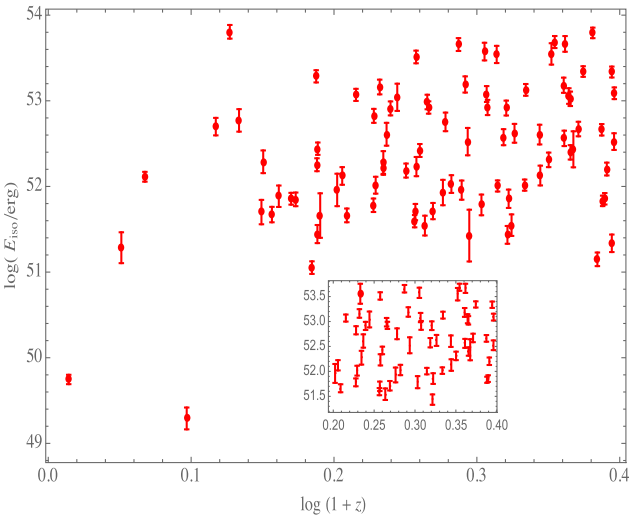

Figure 12. Redshift distribution of $\log E_{\rm iso}/({\rm erg})$ for the subsample used for our calibration.

based on an approximate function for the luminosity distance. This function $d_L^{\rm app}(z)$ has the form

$$d_L^{\rm app}(z) = \frac{c}{H_0}\frac{z(z+1)^2}{\sqrt{d_3 z^3 + \left(d_2 z^2 + d_1 z + 1\right)^2}}, \tag{37}$$

where d_1, d_2, and d_3 are constants. To estimate these parameters, we have simultaneously fitted the SNIa samples and the $H(z)$ measurements. Actually it turns out that we can determine an approximate function for the $H(z)$, from $d_L^{\rm app}(z)$, according to the relation:

$$\frac{1}{H^{\rm app}(z)} = \frac{\rm d}{{\rm d}z}\left(\frac{d_L^{\rm app}(z)}{1+z}\right). \tag{38}$$

We find that $d_1 = 1.18 \pm 0.03$, $d_2 = 0.30 \pm 0.04$, $d_3 = 0.49 \pm 0.1$. In Fig. 13, we plot the data with the best-fitting $d_L^{\rm app}$ and $H^{\rm app}(z)$, respectively.

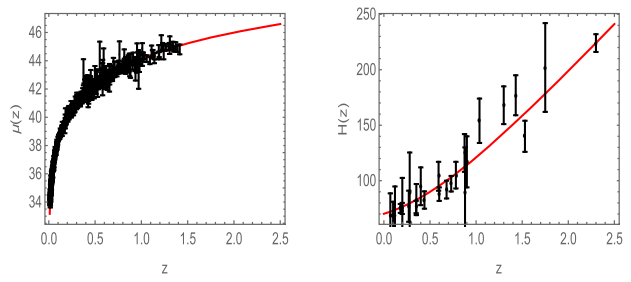

Figure 13. Comparison between the observational data and theoretical predictions for the distance modulus (left-hand panel), and the Hubble function, $H(z)$, (right-hand panel).

Therefore we can use the approximate function $d_L^{\rm app}(z)$ to calibrate the $E_{\rm p,\,i} - E_{\rm iso}$ correlation, following the procedure described above. Using all the data, we find that $a = 1.84 \pm 0.08$, $b = 52.7 \pm 0.05$, $\sigma_{\rm int} = 0.37 \pm 0.04$, $\gamma = 0.03 \pm 0.1$. As the last check we applied the same filters on $E_{\rm p,\,i}$ and $E_{\rm iso}$ as before, selecting a subsample of 128 GRBs, and calibrated the $E_{\rm p,\,i} - E_{\rm iso}$ correlation. We find that $a = 1.94 \pm 0.09$, $b = 52.4 \pm 0.04$, $\sigma_{\rm int} = 0.38 \pm 0.05$, $\gamma = 0.02 \pm 0.15$. Also in this case it turns out that the calibration parameters a, γ and $\sigma_{\rm int}$ are fully consistent with our SNIa-calibration technique, and that all the possible systematics and evolutionary effects are within the intrinsic dispersion $\sigma_{\rm int}$, as already discussed in literature (see for instance, Amati et al. 2008; Amati & Della Valle 2013; Amati & Dichiara 2013). However it is worth noting that when future GRB missions will substantially increase the number of GRBs usable to construct the $E_{\rm p,\,i} - E_{\rm iso}$ correlation up to redshift $z \simeq 10$, they may shed new light on the properties of this important correlation.

3.2.3 Building up the Hubble diagram

After fitting the correlation and estimating its parameters, we used them to construct the GRB Hubble diagram. We recall that the luminosity distance of a GRB with redshift z is

$$d_L(z) = \left(\frac{E_{\rm iso}(1+z)}{4\pi\, S_{\rm bolo}}\right)^{1/2}. \tag{39}$$

The uncertainty of $d_L(z)$ was estimated through the propagation of the measurement errors of the pertinent quantities. In particular, recalling that our correlation relation can be written as a linear relation, as in equations (32) and (33), the error on the distance dependent quantity $y = \log\left[\frac{E_{\rm iso}}{1\ {\rm erg}}\right]$ was estimated as

$$\sigma(y) = \sqrt{a^2\sigma_x^2 + \sigma_a^2 x^2 + \sigma_b^2 + \sigma_{\rm int}^2}, \tag{40}$$

where $x = \log\left[\frac{E_{\rm p,i}}{300\ {\rm keV}}\right]$, σ_b is properly evaluated through the equation (36), which implicitly defines b as a function of a and $\sigma_{\rm int}$, and is then added in quadrature to the uncertainties of the other terms entering equation (39) to obtain the total uncertainty. It turns out that

$$5\log d_L(z) = \left(\frac{5}{2}\right)\left\{b + a\log\left[\frac{E_{\rm p,i}}{300\ {\rm keV}}\right] + (\gamma+1)\log(1+z) - \log(4\pi\, S_{\rm bolo}) + \mu_0\right\}, \tag{41}$$

where μ_0 is a normalization parameter. Actually the distance modulus of GRBs are not absolute, thus this cross-calibration parameter is needed to match the GRB Hubble diagram and the one of supernovae. If μ_0 cannot be determined, we can only use the shape of the Hubble Diagram to constrain the cosmological parameters such as Ω_m and Ω_Λ, with no information on H_0, which is degenerate with the μ_0 parameter. It turns out that μ_0 depends on the fiducial cosmological model and its parameters; however in all models considered in our analysis $\mu_0 \simeq 0.4$. In Fig. 14 we plot the GRB Hubble diagram, and in Fig. 15 we show that this diagram matches the Union 2.1 Hubble diagram, then μ_0 has been evaluated for the CPL best-fitting model, discussed above. In order to make this comparison clearer, we use the auxiliary variable $y = \frac{z}{1+z}$, which map the z-range $[0, \infty)$ into the y-interval $[0, 1]$. It turns out that the GRBs are the natural continuation of SNIa in the Hubble diagram. The listed data are available on request to the authors.

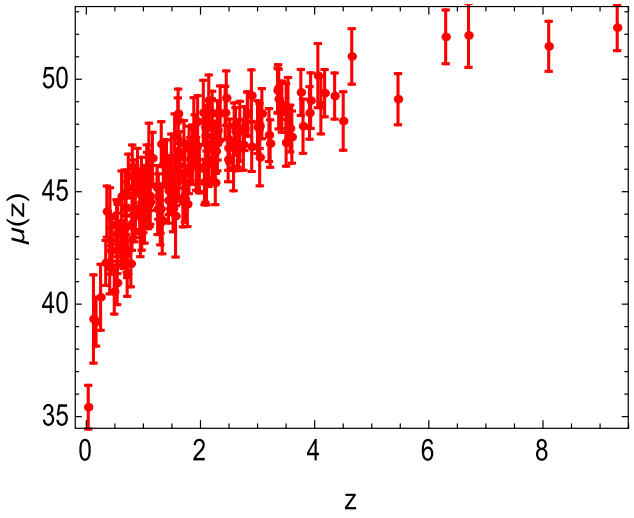

Figure 14. Distance modulus $\mu(z)$ for the calibrated GRB Hubble diagram obtained by fitting the $E_{\rm p,\,i} - E_{\rm iso}$ relation.

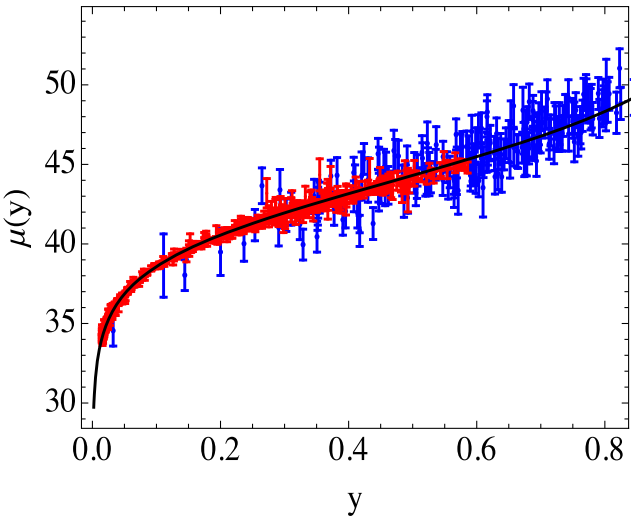

Figure 15. GRB (blue points) and SNIa (red points) superposed Hubble diagrams after μ_0 has been evaluated for the best fit CPL model (see the section below). Here $y = \frac{z}{1+z}$.

3.3 Direct H(z) measurements

The direct measurements of Hubble parameters are complementary probes to constrain the cosmological parameters and investigate the dark energy (Jimenez & Loeb 2002). The Hubble parameter, defined

Table 3. Priors for parameters estimate in the MCMC numerical analysis.

Parameters	Priors
Ω_m	(0, 1)
w_0	(−3, 3)
w_1	(−3, 3)
Ω_e	(0, 0.1)
$\mathcal{H}_0$	(0.5, 1.5)

as $H(z) = \frac{\dot{a}}{a}$, where a is the scale factor, depends on the differential variation of the cosmic time with redshift as

$$H(z) = -\frac{1}{1+z}\left(\frac{\mathrm{d}t}{\mathrm{d}z}\right)^{-1}. \tag{42}$$

The $\left(\frac{\mathrm{d}t}{\mathrm{d}z}\right)$ can be measured using the so-called cosmic chronometers. dz is obtained from spectroscopic surveys with high resolution, and the differential evolution of the age of the Universe dt in the redshift interval dz can be measured provided that optimal probes of the aging of the Universe, that is, the cosmic chronometers, are identified. The most reliable cosmic chronometers observable at high redshift are old early-type galaxies that evolve passively on a time-scale much longer than their age difference, which formed the vast majority of their stars rapidly and early and have not experienced subsequent major episodes of star formation or merging. Moreover, the Hubble parameter can also be obtained from the BAO measurements: by observing the typical acoustic scale in the line-of-sight direction, it is possible to extract the expansion rate of the Universe at a certain redshift. We used a list of 28 direct $H(z)$ measurements in the redshift range $z \sim 0.07 - 2.3$ compiled by Farooq & Ratra (2013).

4 STATISTICAL ANALYSIS

To test the dark energy models described above, we use a Bayesian approach based on the MCMC method. In order to set the starting points for our chains, we first performed a preliminary and standard fitting procedure to maximize the likelihood function $\mathcal{L}(\mathbf{p})$:

$$\mathcal{L}(\mathbf{p}) \propto \frac{\exp\left(-\chi^2_{\mathrm{SNIa/GRB}}/2\right)}{(2\pi)^{\frac{\mathcal{N}_{\mathrm{SNIa/GRB}}}{2}}|\mathbf{C}_{\mathrm{SNIa/GRB}}|^{1/2}} \times \frac{\exp\left(-\chi^2_H/2\right)}{(2\pi)^{\mathcal{N}_H/2}|\,\mathbf{C}_H|^{1/2}}. \tag{43}$$

Here

$$\chi^2(\mathbf{p}) = \sum_{i,j=1}^{N}\left(x_i - x_i^{\mathrm{th}}(\mathbf{p})\right)\mathbf{C}_{ij}^{-1}\left(x_j - x_j^{\mathrm{th}}(\mathbf{p})\right), \tag{44}$$

$\mathbf{p}$ is the set of parameters, N is the number of data points, x_i is the i-th measurement; $x_i^{\mathrm{th}}(\mathbf{p})$ indicate the theoretical predictions for these measurements that depend on the parameters $\mathbf{p}$. C_{ij} is the covariance matrix (specifically, $\mathbf{C}_{\mathrm{SNIa/GRB/H}}$ indicates the SNIa/GRBs/H covariance matrix). equation (43) includes σ_{int} term to allow for intrinsic scatter in the data sets.

In our analysis, we include only flat priors on the typical parameters of the considered cosmological models (see Table 3, with the exception of the Hubble constant, h, for which we consider a Gaussian prior accounting for the local determination of the Hubble constant by the SHOES collaboration $(h_S, \sigma_S) = (0.742, 0.036)$ Riess et al. (2009). We actually consider the term :

$$\mathcal{L}(\mathbf{h}) = \frac{\exp\left[-(h_S - h)^2/4\sigma_S^2\right]}{\sqrt{4\pi\sigma_S^2}}. \tag{45}$$

We sample the space of parameters by running five parallel chains and use the Gelman–Rubin diagnostic approach to test the convergence. As a test probe, it uses the reduction factor R, which is the square root of the ratio of the variance between-chains and the variance within-chain. A large R indicates that the between-chains variance is substantially greater than the within-chain variance, so that a longer simulation is needed. We require that R converges to 1 for each parameter. We set $R - 1$ of the order of 0.05, which is more restrictive than the often used and recommended value $R - 1 < 0.1$ for standard cosmological investigations. We discarded the first 30 per cent of the point iterations at the beginning of any MCMC run, and thinned the chains that were run many times. We finally extracted the constrains on cosmographic parameters by coadding the thinned chains. The histograms of the parameters from the merged chains were then used to infer median values and confidence ranges. In Tables 4, 5, and 6 we present the results of our analysis. In Fig. 16 we plot a 2D confidence region for the CPL model: it is worth noting that, using only the GRB Hubble diagram and the $H(z)$ sample, the ΛCDM model of dark energy is disfavoured at more than 3σ, as indicated also by the Hubble diagram of quasars at high redshifts (Lusso & Risaliti 2017; Risaliti & Lusso 2019). In Figs. 17 and 18 we plot the redshift behaviour of the effective early dark energy (EDE) EOS, and the Ω parameter, corresponding to the best-fitting values obtained in our statistical analysis.

It is well known that the likelihood-statistics alone does not provide an effective way to compare different cosmological models. In this section, we compare the different models presented in the previous sections and check if we can discriminate between them. We use the Akaike Information Criterion (AIC) (Akaike 1974), (Liddle 2007), and its indicator

$$\mathrm{AIC} = -2\ln\mathcal{L}_{\mathbf{max}} + 2n_p + \frac{2n_p(n_p+1)}{N_{\mathrm{tot}} - n_p - 1}, \tag{46}$$

where N_{tot} is the total number of data and n_p the number of free parameters (of the cosmological model). It turns out that the lower is the value of AIC the better is the fit to the data. To compare different cosmological models we introduce the difference $\Delta_{\mathrm{AIC}} = \mathrm{AIC}_{\mathrm{model}} - AIC_{\mathrm{min}}$. This difference corresponds to different cases: $4 < \Delta_{\mathrm{AIC}} < 7$ indicates a positive evidence against the model with higher value of AIC_{model}, while $\Delta_{AIC} \geq 10$ indicates a strong evidence. $\Delta_{AIC} \leq 2$ is an indication that the two models are consistent. In our case we have found that the model with the lower AIC is the exponential scalar field: it turns out that $\Delta_{AIC} \simeq 5$ if we consider the CPL model and $\Delta_{AIC} = 9$ for the early dark energy. Moreover, it turns out that also without the SNIa data, combining the GRB Hubble diagram with the $H(z)$ compilation, it is possible to set the transition region from the decelerated to the accelerated expansion in all the tested cosmological models, as indicated in Figs 19–21.

5 PROSPECTS WITH *THESEUS*

So far we have shown that the $E_{\mathrm{p,\,i}} - E_{\mathrm{iso}}$ correlation has significant implications for the use of GRBs in cosmology and therefore GRBs are powerful cosmological probe, complementary to other probes. GRB missions, like, the proposed *THESEUS* observatory (Amati et al. 2018; Cordier et al. 2018), will substantially increase the number of GRBs that could be used to construct the $E_{\mathrm{p,\,i}} - E_{\mathrm{iso}}$ correlation up to redshift $z \simeq 10$ and will allow a better calibration of

Table 4. Constrains on the CPL parameters from different data: combined SNIa and GRB Hubble diagrams, and $H(z)$ data sets (left-hand panel); and GRB Hubble diagram and $H(z)$ data sets (right-hand panel). Columns show the mean $\langle x\rangle$ and median $\tilde{x}$ values and the 68 per cent and 95 per cent confidence limits.

	CPL dark energy							
Id	$\langle x\rangle$	$\tilde{x}$	68 per cent CL	95 per cent CL	$\langle x\rangle$	$\tilde{x}$	68 per cent CL	95 per cent CL
	SNIa /GRBs/H(z)				GRBs/H(z)			
Ω_m	0.29	0.29	(0.28, 0.30)	(0.27, 0.31)	0. 17	0.18	(0.16, 0.195)	(0.15, 0.26)
w_0	-1.03	-1.02	$(-1.1, -0.96)$	$(-1.14, -0.88)$	-0.84	-0.858	$(-0.94, -0.74)$	$(-1.07, -0.68)$
w_1	0.03	0.03	$(-0.15, 0.24)$	$(-0.32, 0.38)$	0.8	0.86	(0.63, 0.95)	(0.39, 0.99)
h	0.69	0.69	(0.68, 0.70)	(0.67, 0.71)	0.67	0.67	(0.65, 0.7)	(0.62, 0.74)

Table 5. Constrains on the scalar field parameters from different data: combined SNIa and GRB Hubble diagrams, and $H(z)$ data sets (left-hand panel); and GRB Hubble diagram and $H(z)$ data sets (right-hand panel). Columns show the mean $\langle x\rangle$ and median $\tilde{x}$ values and the 68 per cent CL and 95 per cent CL confidence limits. It is worth noting that $\Omega_m = 0.24 \pm 0.02$ in the case of the SNIa /GRBs/H(z) samples, and $\Omega_m = 0.25 \pm 0.03$ for the GRBs/H(z) samples.

	Scalar field quintessence							
Id	$\langle x\rangle$	$\tilde{x}$	68 per cent CL	95 per cent CL	$\langle x\rangle$	$\tilde{x}$	68 per cent CL	95 per cent CL
	SNIa /GRBs/H(z)				**GRBs/H(z)**			
$\mathcal{H}_0$	0.98	0.98	(0.97, 1.0)	(0.95, 1.03)	0. 97	0.98	(0.96, 1.05)	(0.95, 1.1)
h	0.69	0.69	(0.68, 0.70)	(0.67, 0.71)	0.67	0.67	(0.65, 0.7)	(0.62, 0.74)

Table 6. Constrains on the Early Dark Energy parameters from different data: combined SNIa and GRB Hubble diagrams, and $H(z)$ data sets (left-hand panel); and GRB Hubble diagram and $H(z)$ data sets (right-hand panel). Columns show the mean $\langle x\rangle$ and median $\tilde{x}$ values and the 68 per cent CL and 95 per cent CL confidence limits.

	Early dark energy							
Id	$\langle x\rangle$	$\tilde{x}$	68 per cent CL	95 per cent CL	$\langle x\rangle$	$\tilde{x}$	68 per cent CL	95 per cent CL
	SNIa /GRBs/H(z)				GRBs/H(z)			
Ω_m	0.28	0.28	(0.26, 0.30)	(0.25, 0.32)	0. 17	0.18	(0.16, 0.195)	(0.15, 0.26)
w_0	-0.62	-0.6	$(-0.7, -0.53)$	$(-0.95, -0.5)$	-0.84	-0.858	$(-0.94, -0.74)$	$(-1.07, -0.68)$
Ω_e	0.003	0.003	(0.001, 0.07)	(0.005, 0.09)	0.008	0.009	(0.0006, 0.0095)	(0.0004, 0.0015)
h	0.71	0.71	(0.7, 0.72)	(0.69, 0.73)	0.67	0.67	(0.65, 0.7)	(0.62, 0.74)

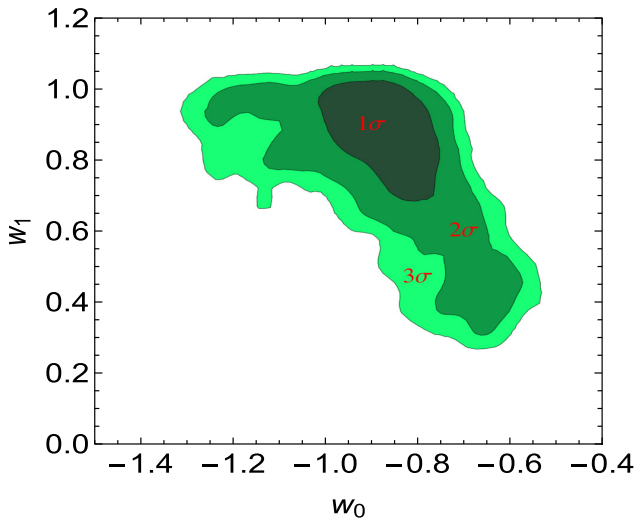

Figure 16 2D confidence regions in the w_0-w_1 plane for the CPL model, obtained from the GRB Hubble diagram and the H(z) sample. It is worth noting that the ΛCDM model of dark energy is disfavoured at more than 3 σ.

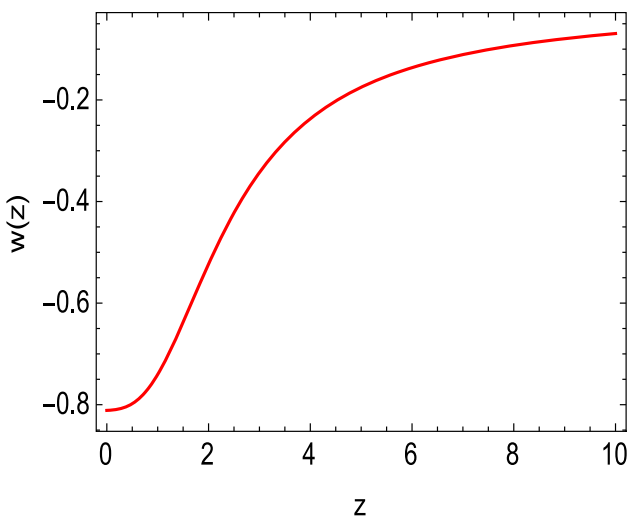

Figure 17. Redshift dependence of the EDE EOS corresponding to the best-fitting values of the parameters.

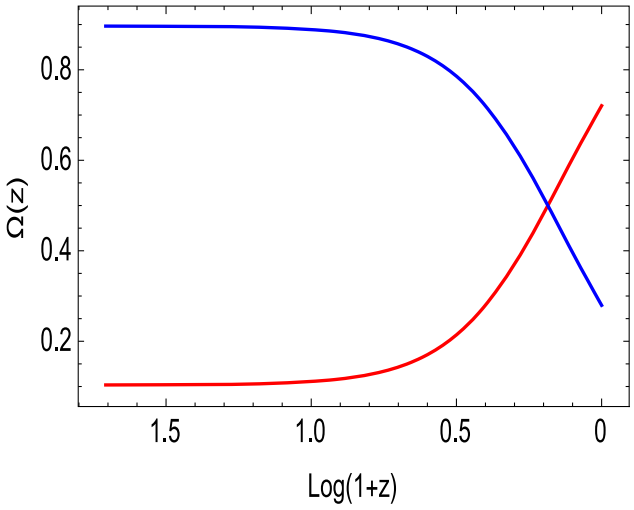

Figure 18. Redshift dependence of the Ω parameters for the EDE model corresponding to the best-fitting values of the parameters: $\Omega_m(z)$ is shown in blue, and $\Omega_{DE}(z)$ in red.

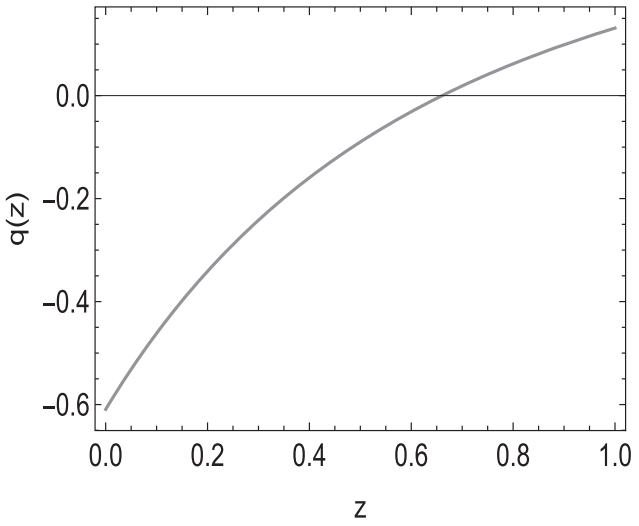

Figure 19. Redshift dependence of the deceleration parameter $q(z)$ for the CPL model, corresponding to the best values of the relative parameters obtained combining the GRB Hubble diagram and the $H(z)$ measurements.

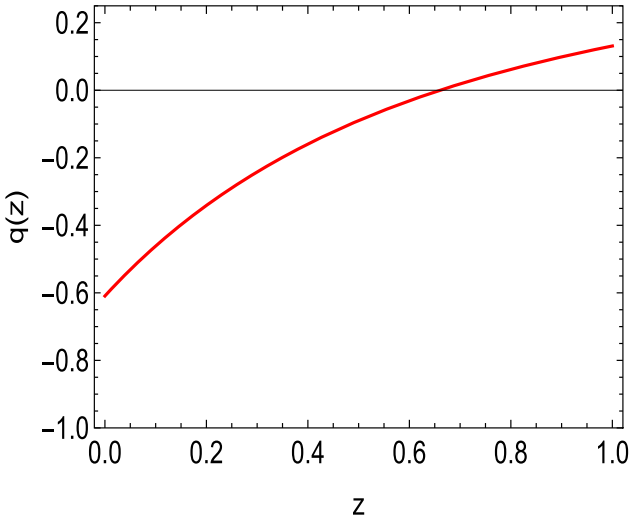

Figure 20. Redshift dependence of the deceleration parameter $q(z)$ for the scalar field model, corresponding to the best values of the relative parameters obtained combining the GRB Hubble diagram and the $H(z)$ measurements.

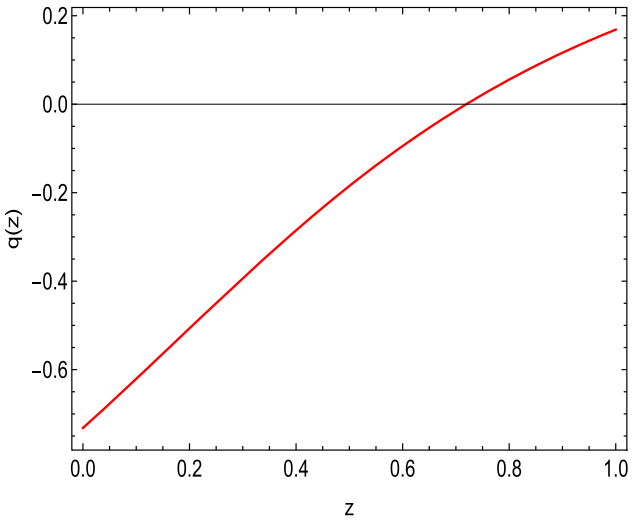

Figure 21. Redshift dependence of the deceleration parameter $q(z)$ for the EDE model, corresponding to the best values of the relative parameters obtained combining the GRB Hubble diagram and the $H(z)$ measurements.

this correlation. Here we consider a simulated sample of 772 objects to constrain our models, their redshift distribution is shown in Fig. 22.

These simulated data sets have been obtained by implementing the Monte Carlo approach and taking into account the slope, normalization, dispersion of the observed $E_{\rm p,\,i}$ and $E_{\rm iso}$ correlation, the distribution of the uncertainties in the measured values of $E_{\rm p,\,i}$ and $E_{\rm iso}$, and finally the observed redshift distribution of GRBs. In this simulations, we took into account the sensitivity limits and spectroscopy thresholds and sensitivity of the *THESEUS* monitors (SXI and XGIS). This mock sample is based on parameters of the observed sample and corresponds to the actual data sets and to the data sets expected to be available within 3–4 yr from *THESEUS*. The cosmological parameters assumed for the simulations are the median, or average, values found in the reported analysis on real data and, indeed, Tables (7) and (8) show that the analysis on the simulated data recover very well these assumed cosmological parameters. It turns

Table 7. Constrains on the CPL parameters from our simulated GRB Hubble diagram and $H(z)$ data.

			CPL dark energy	
Id	$\langle x\rangle$	$\tilde{x}$	68 per cent CL	95 per cent CL
			Simulated GRBs/H(z)	
Ω_m	0.18	0.19	(0.16, 0.21)	(0.15, 0.27)
w_0	−0.86	−0.86	(−0.94, −0.79)	(−1.07, −0.72)
w_1	0.82	0.82	(0.71, 0.93)	(0.62, 0.98)
h	0.67	0.67	(0.65, 0.69)	(0.61, 0.74)

out that with our mock sample of GRBs we are able to constrain much better the cosmological parameters. Actually, in Figs 23–25, we show the 2D confidence regions in the w_0–w_1 plane for the CPL model, obtained from the simulated GRB Hubble diagram and the $H(z)$ sample, compared with the same confidence region obtained from the

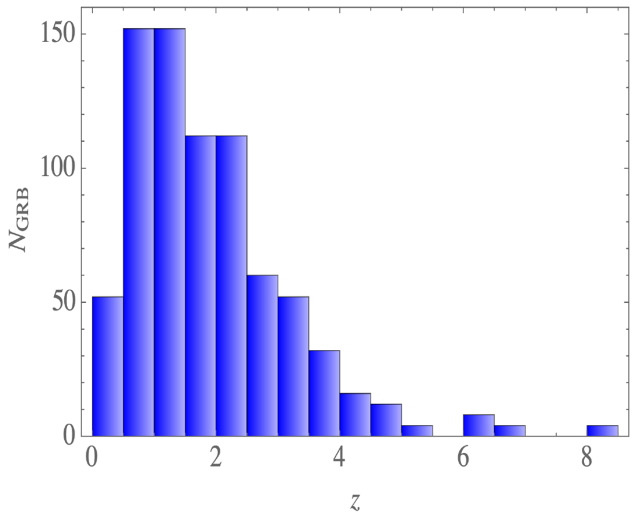

Figure 22. Simulated data for a *THESEUS 24like* like mission: we plot the GRB redshift distribution of the sample of 772 GRBs used in our analysis.

Table 8. Constrains on the scalar field parameters from our simulated GRB Hubble diagram and $H(z)$ data. It turns out that $\Omega_m = 0.26 \pm 0.02$.

	Scalar field quintessence			
Id	$\langle x \rangle$	$\tilde{x}$	68 per cent CL	95 per cent CL
	Simulated GRBs/H(z)			
$\mathcal{H}_0$	0.98	0.981	(0.96, 1.00)	(0.94, 1.02)
h	0.68	0.68	(0.68, 0.69)	(0.65, 0.70)

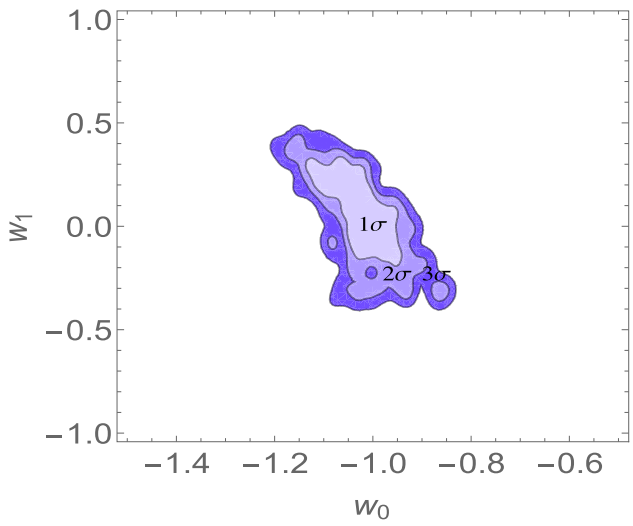

Figure 23. 2D confidence regions in the w_0–w_1 plane for the CPL model, obtained from the full real data sets.

real data sets, it turns out that the evolving dark energy, described by the exponential scalar field potential is the favoured model. Moreover, in the case of the CPL model, we tested the efficiency of our probes looking at the Figure of Merit (FoM), that is the inverse of area of the $w_0 - w_1$ contour: for this purpose we simulate new mock samples of the CPL cosmological model corresponding to the best-fitting values in Table 7, with the probability density function for the distribution in redshift corresponding to the histograms in Figs 22 and 26, and

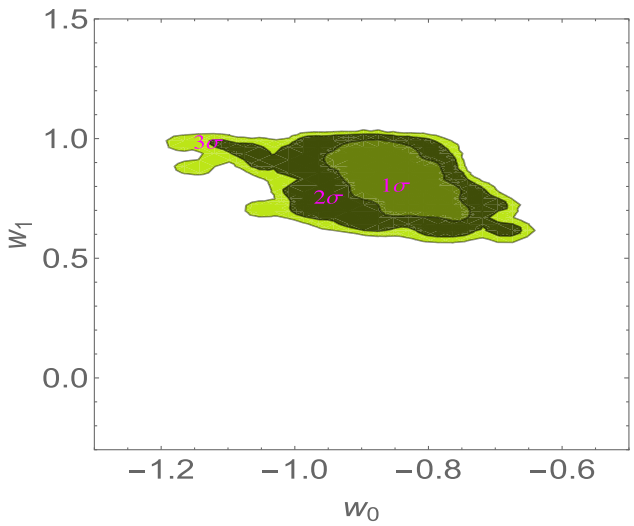

Figure 24. 2D confidence regions in the w_0–w_1 plane for the CPL model, obtained from the simulated GRBs HD and the $H(z)$ measurements (bottom panel) and the full real data sets (upper panel).

containing respectively 772 and 1500 objects. To each simulated GRB we estimate the error on the distance modulus as:

$$\sigma_\mu(z) = \sqrt{\sigma_{\rm sys}^2 + \left(\frac{z}{z_{\rm max}}\right)^2 \sigma_m^2}. \quad (47)$$

Here $z_{\rm max}$ is the maximum redshift of the sample, and $\sigma_{\rm sys}$ the intrinsic scatter. In our case $(z_{\rm max}, \sigma_{\rm sys}, \sigma_m) = (8.5, 0.3, 0.05)$. We get $FoM = 1.9$ when using 772 GRBs, and it increases up to $FoM = 4.8$ if 1500 GRBs are used, thus confirming that with future data we will able to better constrain the dark energy EOS as described by the CPL parametrization.

6 DISCUSSION AND CONCLUSIONS

The $E_{\rm p,\,i} - E_{\rm iso}$ correlation has significant implications for the use of GRBs in cosmology to test different models of dark energy beyond the standard ΛCDM. Here we considered an *extended* $E_{\rm p,\,i} - E_{\rm iso}$ correlation, which takes into account possible redshift evolution effects (related, for instance to the gravitational lensing along the GRB line of sight), parametrized as power-law terms. Using recently updated data set of 193 high-redshift GRBs, we applied a local regression technique to calibrate the $E_{\rm p,\,i} - E_{\rm iso}$ relation. The values of the calibration parameters are statistically fully consistent with the results of our previous work (Demianski et al. 2011, 2017a), and confirm that for this correlation the evolution effects remain within the intrinsic scatter of the correlation around the best-fitting values, $\sigma_{\rm int}$. This result has been confirmed also with different calibration techniques, based on an approximation function able to reproduce the luminosity distance in different cosmological models. Moreover in order to further investigate this question here we follow a different approach: in order to remove possible systematics, we apply some filters on the $E_{\rm p,\,i} - E_{\rm iso}$ correlation, selecting a subsample where they are homogeneously distributed in the redshift space and we showed that none of the measured values of $E_{\rm p,\,i} - E_{\rm iso}$ are systematically larger at lower redshifts than at higher redshifts. Again we fit the calibration within this smaller sample, and the results are fully consistent with the results obtained on the whole data set. Therefore these results justify extension of this calibration to the whole sample, at least on the basis of the current stage of knowledge. The fitted calibration parameters have been used to construct a high redshift

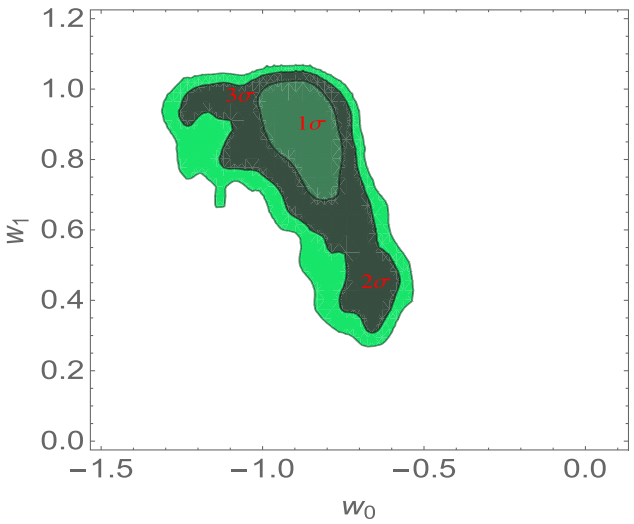

Figure 25. 2D confidence regions in the w_0–w_1 plane for the CPL model, obtained from the GRBs HD and the $H(z)$ measurements.

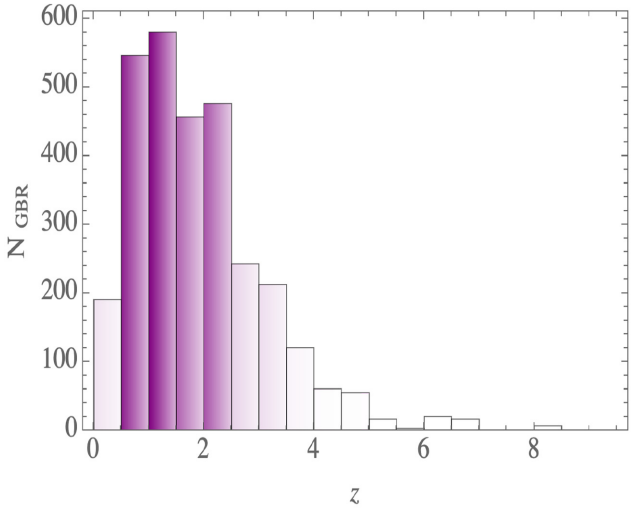

Figure 26. Simulated data for a *THESEUS*-like mission: we plot the GRB redshift distribution of the sample of 1500 GRBs used in our analysis.

GRB Hubble diagram, which we adopted as a tool to constrain different cosmological models: to investigate the prospective for high redshift constrains on dark energy models with the $E_{\rm p,\,i} - E_{\rm iso}$ correlation is the prime objective of our analysis. We considered the CPL parametrization of the EOS, an exponential potential of a self-interacting scalar field, and, finally a model with dark energy at early times. We compare these different models, by using the AIC and its indicator. In our case we have found that the model with the lower AIC is the exponential scalar field: $\Delta_{AIC} \simeq 5$ if we consider the CPL model and $\Delta_{AIC} = 9$ for the early dark energy. Therefore this model is slightly preferred by the present data. Moreover, even if the cosmological constrains from the currently available GRB Hubble diagram are not so restrictive, future GRB missions, like the proposed *THESEUS* observatory will increase the number of GRB usable to construct the $E_{\rm p,\,i} - E_{\rm iso}$ correlation up to redshift $z \simeq 10$. We actually considered a mock sample, consisting of 772 objects, obtained taking into account the slope, normalization, dispersion of the observed correlation, the distribution of the uncertainties in the measured values of $E_{\rm p,\,i}$ and $E_{\rm iso}$, and finally the observed redshift distribution of GRBs. In these simulations, we took into account the sensitivity limits and spectroscopy thresholds and sensitivity of the *THESEUS* monitors. The mock sample corresponds to the data sets expected to be available within few years from *THESEUS*. It turns out that in this case we are able to constrain much better the cosmological parameters, and the exponential scalar field potential is confirmed as the favourite model. We finally tested the efficiency of our probes looking at the Figure of Merit (FoM). In the case of the CPL model: we simulated new mock samples consisting of 772 and 1500 objects respectively, and we get $FoM = 1.9$ when using 772 GRBs, while it increases by a factor 2.5 if 1500 GRBs are used. This confirms, indeed, that with future data we will be able to better constrain the evolution of the dark energy EOS, in a complementary way to type Ia SN, and in synergy with other independent high redshift cosmological probes, as, for instance quasars (Lusso 2020; Lusso et al. 2020).

ACKNOWLEDGEMENTS

MD is grateful to the INFN for financial support through the Fondi FAI GrIV. EP acknowledges the support of INFN Sez. di Napoli (Iniziativa Specifica QGSKY). LA acknowledges support by the Italian Ministry for Education, University, and Research through PRIN MIUR 2009 project on 'Gamma ray bursts: from progenitors to the physics of the prompt emission process.' (Prot. 2009 ERC3HT).

DATA AVAILABILITY

The data underlying this article will be shared on reasonable request to the corresponding author.

REFERENCES

Amati L. et al., 2018, Advances in Space Research, 62, 191
Cordier B., Götz D., Motch C., SVOM Collaboration, 2018, Mem. SAIt, 89, 26
Akaike H., 1974, IEEE Trans. Automatic Control, 19, 716
Alam U., Sahni V., Saini T. D., Starobinsky A. A., 2003, MNRAS, 344, 1057
Alcaniz J. S., Lima J. A. S., 2001, ApJ, 550, L133
Amanullah R. et al., 2010, ApJ, 71, 712
Amati L., Della Valle M., 2013, Int. J. Mod. Phys. D, 22, 1330028
Amati L., Dichiara S., 2013, Acta Polytech., 53, 687
Amati L., et al. 2002, A&A, 390, 81
Amati L., Guidorzi C., Frontera F., Della Valle M., Finelli F., Landi R., Montanari E., 2008, MNRAS, 391, 577
Amati L., Frontera F., Guidorzi C., 2009, A&A, 508, 173
Amati L., Sawant D., Della Valle M., 2016a, Astron. Astrophys. Trans., 29, 193
Amati L., D'Agostino R., Luongo O., Muccino M., Tantalo M., 2019, MNRAS, 486, L46
Astier P. et al., 2006, A&A, 447, 31
Band D., 1993, ApJ, 413, 281
Band D., Preece R., 2005, ApJ, 627, 319
Basak R., Rao A. R., 2013, ApJ, 775, 31
Bueno Sanchez J. C., Perivolaropoulos L., 2010, Phys. Rev. D, 81, 103505
Caldwell R. R., Dave R., Steinhardt P. J., 1998, Phys. Rev. Lett., 80, 1582
Cao S., Ryan J., Khadka N., Ratra B., 2021, MNRAS, 501, 1520
Capozziello S., De Laurentis M., 2011, Phys. Rep., 509, 167
Capozziello S., Cardone V. F., Piedipalumbo E., Rubano C., 2006, Class. Quatum Gravity, 23, 1205
Capozziello S., D'Agostino R., Luongo O., 2019, Int. J. Mod. Phys. D, 28, 1930016
Carroll S. M., 2001, Living Rev. Relat., 4, 1

Chevallier M., Polarski D., 2001, Int. J. Mod. Phys. D, 10, 213
Clarkson C., Maartens R., 2010, Class. Quantum Gravity, 27, 124008
Clifton T., Ferreira P. G., Padilla A., Skordis C., 2012, Phys. Rep., 513, 1
Copeland E. J., Sami M., Tsujikawa S., 2006, Int. J. Mod. Phys. D, 15, 1753
Dainotti M. G., Amati L., 2018, PASP, 987, 051001
Dainotti M. G., Postnikov S., Hernandez X., Ostrowski M., 2016, ApJ, 825, L20
Das S. et al., 2011, Phys. Rev. Lett., 107, 021301
De Felice A., Tsujikawa S., 2010, Living Rev. Rel., 13, 3
Demianski M., Piedipalumbo E., 2011, MNRAS, 415, 3580
Demianski M., Piedipalumbo E., Rubano C., Tortora C., 2005, A&A, 431, 27
Demianski M., Piedipalumbo E., Rubano C., Scudellaro P., 2008, A&A, 481, 279
Demianski M., Piedipalumbo E., Rubano C., 2011, MNRAS, 411, 1213
Demianski M., Piedipalumbo E., Sawant D., Amati L., 2017a, A&A, 598, A112
Demianski M., Piedipalumbo E., Sawant D., Amati L., 2017b, A&A, 598, A113
Di Valentino E., 2021, MNRAS, 502, 2065
Doran M., Robbers G., 2006, J. Cosmol. Astropart. Phys., 06, 026
Doran M., Lilley M., Wetterich C., 2002, Phys. Lett. B, 528, 175
Fana Dirirsa F. et al., 2019, ApJ, 887, 13
Farooq O., Ratra B., 2013, ApJ, 766, L7
Frontera F. et al., 2013, ApJ, 754, 138
Ghirlanda G., Ghisellini G., Firmani C., Lazzati D., 2004, ApJ, 616, 331
Ghirlanda G., Nava L., Ghisellini G., Firmani C., Cabrera J. I., 2008, MNRAS, 387, 319
Ghirlanda G., Nava L., Ghisellini G., 2010, A&A, 511, 43
Gruber D., 2012, Rest-frame properties of gamma-ray bursts observed by the Fermi Gamma-Ray Burst Monitor, in PoS, Proceedings of Science, SISSA, 34136 Trieste ITALY. p. 7
Izzo L., Muccino M., Zaninoni E., Amati L., Della Valle M., 2015, A&A, 582, A115
Jimenez R., Loeb A., 2002, ApJ, 573, 37
Karwal T., Kamionkowski M., 2016, Phys. Rev. D, 94, 103523
Khadka N., Ratra B., 2020, MNRAS, 499, 391
Khoraminazad H, Viel M., Baccigalupi C., Archidiacono M., 2020, J. Cosmol. Astropart. Phys., 7, 39
Kodama Y., Yonetoku D., Murakami T., Tanabe S., Tsutsui R., Nakamura T., 2008, MNRAS, 391, L1
Liang N., Xiao W. K., Liu Y., Zhang S. N., 2008, ApJ, 685, 354
Liddle A. R., 2007, MNRAS, 377, L74
Linder E. V., 2003, Phys. Rev. Lett., 90, 091301
Lin H.-N., Li X., Liu Y., Wang S., Chang Z., 2015, MNRAS, 453, 128
Lin H.-N., Li X., Chang Z., 2016a, MNRAS, 459, 2501
Lin H.-N., Li X., Chang Z., 2016b, MNRAS, 455, 2131
Lu R., et al., 2012, ApJ, 756, 112
Luongo O., Muccino M., 2021, MNRAS, 503, 4581
Lusso E., 2020, Front. Astron. Space Sci., 7, 8
Lusso E., Risaliti G., 2017, A&A, 602, A69
Lusso E., Piedipalumbo E., Risaliti G., Paolillo M., Bisogni S., Nardini E., Amati L., 2019, A&A, 628, L4
Lusso E. et al., 2020, A&A, 642, A150
Ma C., Caldwell R. R., Bode P., Wang L., 1999, ApJ, 521, L1
Maeda K., 1989, Phys. Rev. D, 39, 3159
Martone R., Izzo L., Della Valle M., Amati L., Longo G., Gotz D., 2017, A&A, 608, A52
Montiel A., Cabrera J. I., Hidalgo J. C., 2021, MNRAS, 501, 3515
Muccino M. et al., 2021, ApJ, 908, 181
Nakar E., Piran T., 2005, MNRAS, 360, L73
Nava L., Ghirlanda G., Ghisellini V., Celotti A., 2011, A&A, 530, 21
Nesseris S., Perivolaropoulos L., 2005, Phys. Rev. D, 72, 123519
Niedermann F., Sloth M. S., 2020, Phys. Rev. D, 102, 063527
Peebles P. J. E., 1984, ApJ, 284, 439
Peebles P. J. E., Ratra B., 1988a, ApJ, 325, 17
Perlmutter S. et al., 1998, Nature, 391, 51
Perlmutter S. et al., 1999, ApJ, 517, 565
Pettorino V., Amendola L., Wetterich C., 2013, Phys. Rev. D, 87, 083009
Piedipalumbo E., Scudellaro P., Esposito G., Rubano C., 2012, Gen. Relativ. Gravit., 44, 2611
Planck Collaboration XIII, 2016, A&A, 594, A13
Ratra B., Peebles P. J. E., 1988b, Phys. Rev. D, 37, 3406
Riess A. G. et al., 1998, AJ, 116, 1009
Riess A. G. et al., 2007, ApJ, 659, 98
Riess A. G. et al., 2009, ApJ, 699, 539
Risaliti G., Lusso E., 2019, Nat. Astron., 3, 272
Rubano C., Scudellaro P., 2002, Gen. Relativ. Gravit., 34, 307
Sahni V., Saini T. D., Starobinsky A. A., Alam U., 2003, J. Exp. Theor. Phys. Lett., 77, 201
Sakamoto T. et al., 2008, ApJS, 175, 179
Sawant D., Amati L., 2018, in Bianchi M., Jansen R. T., Ruffini R., eds, Perspective GRB cosmology with time resolved Ep,i(t)-Liso(t) correlation, The Fourteenth Marcel Grossmann Meeting On Recent Developments in Theoretical and Experimental General Relativity, Astrophysics, and Relativistic Field Theories, held 12-18 July 2015 in Rome. World Scientific Publishing Co. Pte. Ltd., Italy, p. 2913
Shirokov S. I., Sokolov I. V., Lovyagin N. Y., Amati L., Baryshev Y. V., Sokolov V. V., Gorokhov V. L., 2020, MNRAS, 496, 1530
Si S.-K. et al., 2018, ApJ, 863, 50
Suzuki et al. (The Supernova Cosmology Project), 2012, ApJ, 746, 85
Tsujikawa S., 2013, Class. Quantum Gravity, 30, 241003
Ulanov M. V. et al., 2005, Il Nuovo Cimento C, 28, 351
Wang F. Y., Dai Z. G., Liang E. W., 2015, New Astron. Rev., 67, 1
Wei H., 2010, J. Cosmol. Astropart. Phys., 2010, 020
Wei J.-J., Wu X.-F., 2017, Int. J. Mod. Phys. D, 26, 1730002
WMAP Collaboration, 2013, ApJS, 208, 19H
Zhao W. et al., 2020, ApJ, 900, 112

This paper has been typeset from a TEX/LATEX file prepared by the author.